Nuclear Materials Authority
P.O.Box 530 Maadi, Cairo, Egypt

ISSN 2314-5609
Nuclear Sciences Scientific Journal
9A, 131-164
2020
http://www.ssnma.com

INTEGRATION OF LANDSAT-8 AND AIRBORNE GAMMA-RAY SPECTROMETRIC DATA FOR GEOLOGIC MAPPING OF KAB AMIRI AREA, CENTRAL EASTERN DESERT, EGYPT

YASSER S. BADR
Nuclear Materials Authority, El-Maadi, Cairo, Egypt

ABSTRACT

Kab Amiri area in the Central Eastern Desert of Egypt comprises a variety of basement rocks including ophiolitic mélange (serpentinites and metasediments), metavolcanics, older granitoids and younger granites. In this study, Landsat-8 image processing and airborne gamma-ray spectrometric data were integrated to discriminate and mapping lithological units. The applied image processing including Optimum Index Factor and data transformation techniques such as band ratios and principal component analysis in addition to supervised classification were effective in discrimination the different rock units especially the younger granites into two verities. The radioelement maps are correlated with the processed Landsat-8 images to delineate different rock units and their radioactive penalties. They show a limited capability in geological mapping compared with Landsat-8 image processing. They discriminate the younger granites and older granitoids (relatively higher radioactivity) from the other rock units (relatively lower radioactivity), but they failed to discriminate between the two varieties of the younger granites. Gabal Kab Amiri granitic pluton possesses the highest radioactivity in the area relative to the other rock units. Landsat-8 image processing results are confirmed by detailed filed work and petrographic investigation. The petrographic investigation revealed that the younger granites are represented by monzogranites and syenogranites, whereas the older granitoids are represented by granodiorites. A detailed geologic map of scale 1:50,000 is constructed from the interpretation of the processed Landsat-8 images, airborne gamma-ray spectrometry, fieldwork and petrographic studies. Consequently, remote sensing is recommend as a rapid and cost effective tool for mapping lithological units in arid regions.

INTRODUCTION

The basement rocks of Egypt cover about 100.000 km^2 (about 10% of the total area of Egypt). The basement rocks of the Egyptian Eastern Desert is a part of the Arabian Nubian Shield that represent the north eastern part of the U-shaped Pan African orogenic beltand extend through Sudan, South Sudan, Ethiopia, Somalia, Saudi Arabia and Yemen. These rocks were formed in the East African Orogeny during the collision between East and West Gondwana and the closure of the Mozambique Ocean 600 Ma (Stern, 1994 and Kusky and Matsah, 2003). The Eastern Desert is traditionally divided into northern (NED), central (CED), and southern (SED)parts by two rough lines are running from River Nile to Red Sea; a) the first from Qena to Safaga city and b) the second from Idfu to MarsaAlam city. These subdivisions confine parts

with common geographic and lithostructural discontinuities (Stern, 1979 and Abdel Meguid, 1992). The Central Eastern Desert is generally built up of ophiolitic mélange and associated rocks together with subordinate molasse-type sediments and late-tectonic volcanics and granitoid intrusives (El Ramly et al., 1993).

Kab Amiri area is located between lat. 26º18` 11`` and 26º25` 04`` N and long. 33º31` 48`` and 33º40` 06``E in the Central Eastern Desert of Egypt (Fig. 1). It covers an area of about 175 km^2. Three main Wadis,with general NW-SE direction, are traversing the area;Wadi (W.) Kab Amiri, W. Um El Abas and W. Bohlog. Gabal (G.) Kab Amiri represents the highest elevation point in the area about (952m).

Multispectral remote sensing has been broadly used for lithological mapping and mineral exploration especially with the development of their sensors and algorithms (Sabins, 1999; Ferrier et al., 2002; Bishta, 2004;Mars and Rowan 2006; Gad and Kusky, 2006; Zhang et al., 2007; Youssef et al., 2009; Ramadan et al., 2013; Pour and Hashim, 2015; Dawoud et al., 2017; Azzaz et al., 2018; Hammed et al., 2020 and Abdel Ghani, 2020).

The present study aims at integratingthe Landsat-8 image processing, airborne gamma-ray spectrometric data,fieldwork and laboratory investigation to discriminate and mapping lithological units of Kab Amiri area in the Central Eastern Desert (CED) of Egypt.

GEOLOGIC SETTING

The basement rocks in the study area comprise, from the oldest to youngest: ophiolitic mélange (rock fragments of serpentinites in a matrix of metasediments), metavolcanics, older granitoids and younger granites (Fig. 2).

The ophiolitic mélange is comprising serpentinites as blocks set in a metasedimentary matrix and represent the oldest rock unit exposed in the studied area. The serpentinites are cropping out as elongated ridges with general trend E-W and N-S directions at the south and east of the Kab Amiri granitic pluton respectively. They are enveloped by the metasediments (Fig. 3). Serpentinitesare of grayish green color, moderate to high re-

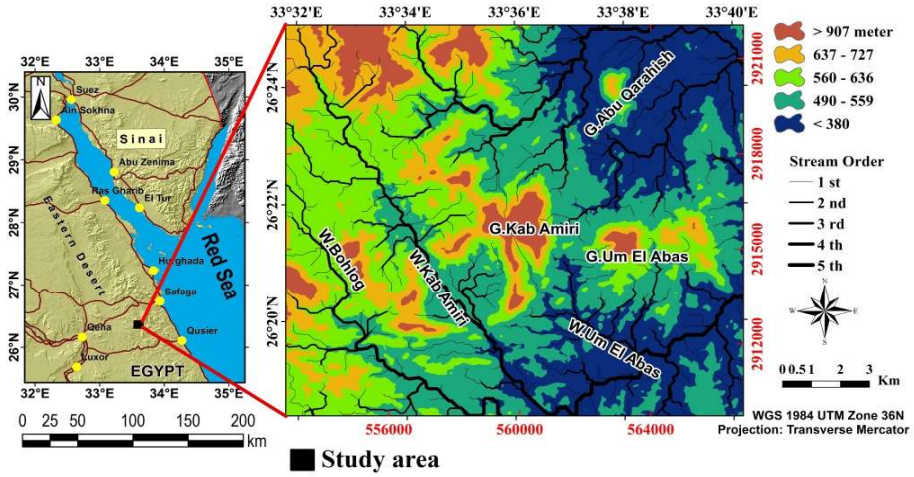

Fig. 1: Location and topographic maps of Kab Amiri area, CED, Egypt

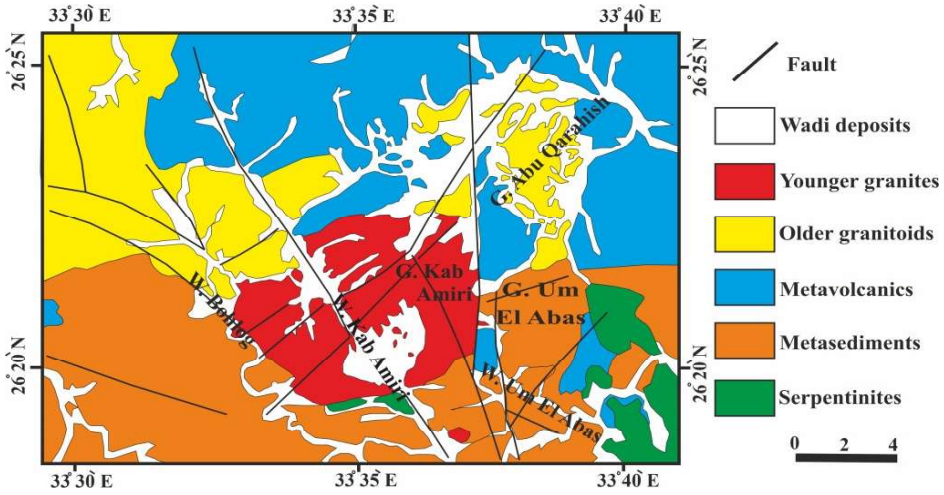

Fig. 2: Geological map of Kab Amiri area, CED, Egypt (Modified after Ammar, 1993)

Fig. 3: Serpentinite rocks (SER) enveloped by metasediments (MS)

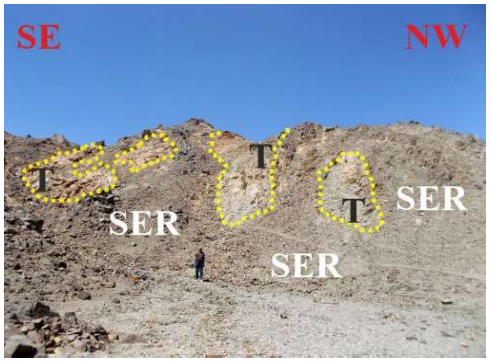

Fig. 4: Serpentinites (SER) altered to talc-carbonate (T)

lief,usually altered to talc-carbonate of dark brown and buff colors (Fig. 4). The metasedimentary rocks are cropping out form a curvilinear belt surrounding the Kab Amiri granitic mass from south. They are mainly fine- to medium-grained, grayish green in color and have low-, to moderate-relief. The highest relief (911m above sea level) is at G. Um El Abas east of G.Kab Amiri. They are mostly foliated, folded and the contacts with the metavolcanic rocks are structural. Several intrusive bodies of younger granites (Fig. 5) invade them.

The metavolcanics are cropping out at the north and northwestern parts of the studied area with general trend (E-W) direction. The metavolcanics are mainly basic in composition (altered metabasalts). These rocks form moderate to high relief ridges, dark grey to greenish grey in color. The metavolcanics are

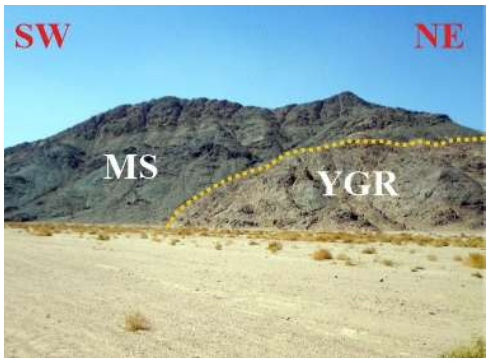

Fig. 5: Sharp contact between metasediments (MS) and younger granite (YGR)

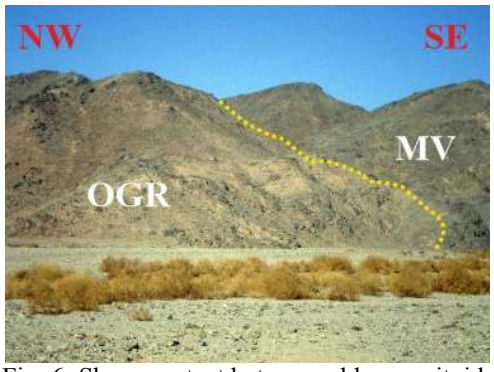

Fig. 6: Sharp contact between older granitoids (OGR) and metavolcanics (MV)

intruded from the southwest by the older granitoids (Fig. 6).

The older granitoids are cropping out in the northwestern part of the mapped area at W. Bohlog-W. Kab Amiri and at G. Abu Qarahish at the northeastern part of the area. G. Abu Qarahish is an oval shaped body about 6×4 km^2. It is elongated in the NNW direction and is cut by a group of basic dykes having NE-SW direction. Generally, the older granitoids are medium-, to coarse-grained and are grey in color. They are intruded into the metavolcanics. These rocks are characterized by the presence of metavolcanic xenoliths (Fig. 7).

Fig. 7: Close up view showing xenoliths of metavolcanic(MV) in older granitoids (OGR)

The younger granites are cropping out in the center of the study area as an oval shaped body about 25 km^2. W. Kab Amiri has general NW-SE trend and separates the pluton into two parts. The field check revealed that the granitic pluton could be distinguished into two concentric zones. The inner zone is medium-, to coarse-grained, whitish pink granite of low relief and highly weathered. It formed of monzogranites with some intrusions of syenogranites. The outer zone is mainly composed of syenogranites with fine-grained size and pink color. Syenogranites are higher in relief and forming conspicuous peaks, the highest onecalled Kab Amiri (952m above sea level). Several pegmatite bodies recorded along the contacts between the syenogranites and the monzogranites in one hand (Fig. 8) and the metasediments on the other hand. These pegmatite lenses exhibit high radioactivity and enclose dark radioactive minerals. Several, nearly parallel, basic dykes with a general trend (NE-SW) direction cut G. Kab Amiri pluton. The pluton is intruding into the metasediments and the metavolcanics (Fig. 9) and carrying several xenoliths of them.

Another rounded shaped younger granitic body (about 0.5km in diameter) are cropping

Fig. 8: Close up view showing pegmatite body

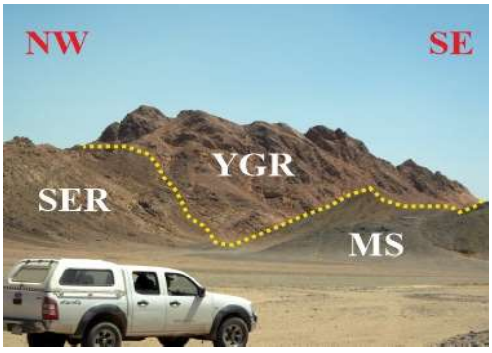

Fig. 10: Sharp contact between younger granite (YGR), metasediments (MS) and serpentinites (SER)

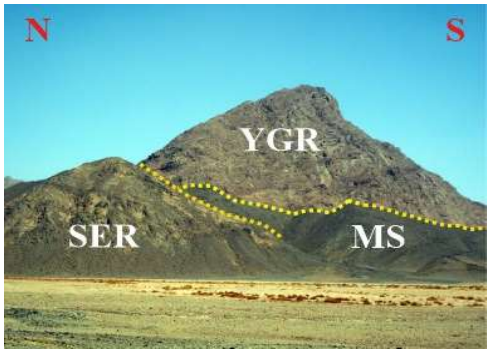

Fig. 9: Sharp contact between younger granite (YGR), metasediments (MS) and serpentinites (SER)

out at the southeastern side of Kab Amiri pluton (Fig. 10). This granitic body is medium-grained, pink to red color, muscovite-bearing granite. The muscovite abundance is however low and may be mainly of secondary origin. It is highly faulted and fractured. A great effect of hydrothermal alteration processes is observed along these fractures. The most effective alteration type is desilicification of the younger granites. This process leads to mineralogical compositions of somewhat similar to that of a syenite (Cathelineau, 1986). The increase of radiometric anomalies increases along these zones of alteration.

MATERIALS AND METHODS

The study area is covered by a single Landsat-8 L1T (terrain corrected) scene (path174 / row 42), free cloud, acquired on July 5, 2019 at 08:12 am local time. Scene is obtained from USGS Earth Explorer site (http://earth explorer.usgs.gov/). The Scene is radiometrically calibrated, atmospherically corrected using the Fast Line of Sight Atmospheric Analysis of Spectral Hypercube (FLAASH) and subset to fit the study area. In this study, only multispectral data (VNIR and SWIR) bands are used. The map projection is Universal Transverse Mercator (UTM) and the datum is WGS 84. ENVI software (version 5.3) is used in the preprocessing and processing of the scene.

Optimum Index Factor (OIF) and other transformation techniques including band ratios (BR) and principal component analysis (PCA) in addition to supervised classification are applied to discriminate different rock units at KabAmiri area. Finally, HIS-RGB image enhancement technique applied for improved visualizing of targets.

Optimum Index Factor is a mathematical algorism used to determine the best (RGB) band combination of the image (Chavez et al., 1982; Sheffield, 1985; Yang et al., 2008 and Pournamdari et al., 2014). The color band

combination in RGB with the highest OIF value have themaximum extractable spectral information since it uses bands with the least redundancy in the data.

Band ratios is a statistical approach used to display spectral variation (Vincent and Thomson, 1972 and Goetz and Rowan, 1981). Band ratios enhance the spectral differences between bands and reduce the effects of topography (ENVI, 2005). Spectral band ratios enhance compositional information while suppressing other types of information about earth's surface, such as terrain slope and grain size differences (Vincent, 1997). Band ratios technique has been used successfully in Geologic mapping by many authors (Sultan et al., 1986; Kaufmann, 1988; Frei and Jutz, 1989; El-Rakaiby, 1993; Sabins, 1999; Abdel salam et al., 2000; Abdeen et al., 2001; Rowan et al., 2003; Velosky et al., 2003; Di Tommaso and Rubinstein 2007; Gabr et al., 2010; Badr, 2017 and Abdel Ghani, 2020). The spectral profiles of the exposed basement rock units of Kab Amiri area that were extracted from OLI data (Fig. 11) were considered the basic criteria for choosing the applied band ratios.

Principal component analysis is a transformation technique reduce multi-dimensional data sets to lower dimensions for analysis and for removing the redundancy of information that exists between the different bands to extract the pertinent information from them (Loughlin, 1991; Gomez et al. 2005).

The airborne gamma-ray spectrometric data of the study area was acquired, in 1984. The survey was carried out along parallel flight lines oriented in a NE-SW direction at one km spacing, while the tie lines were flown in a NW-SE direction at 10 km intervals at a nominal flight altitude of 120 m terrain clearance (Aero-Service, 1984). All the aero-spectrometric data (TC, K, eU and eTh values) are multiplied by 10. The data were processed and resulted in three radio elemental maps of eU, eTh and K. These spectrometric data also treated qualitatively and quantitatively to stand on the radioactive anomalies in the study area. The airborne gamma-ray spectrometric data were processed using Geosoft Oasis Montaj software (version 8.4). The methodology used in this study is summarized on Figure (12).

Fieldworks carried out to verify the processed remote sensing data. Identification of different rock units cropping out in the area and their boundaries has been confirmed.

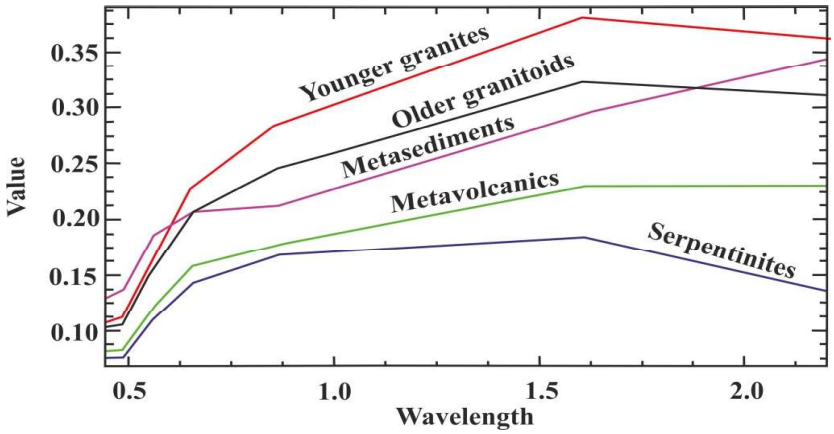

Fig. 11: Spectral signature profiles for the exposed basement rocks of Kab Amiri area, CED, Egypt

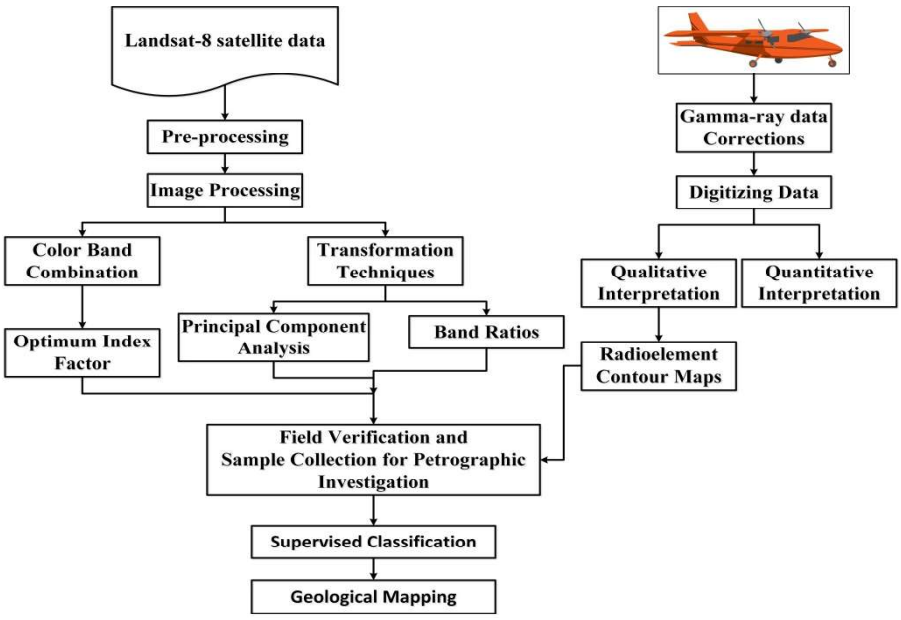

Fig. 12: Flowchart of the main processing steps that performed in the present study

Representative samples from only granitic rockswere collected for petrographic studies.

RESULTS AND DISCUSSION

The spectral differences between rock units were better visually displayed with color composites. There are 35 possible RGB color composite for the 7 reflected bandsof Landsat-8. Selection of the best color composite for visual interpretation and lithological mapping of images was made using a statistical approach known as Optimum Index Factor (OIF). The OIF is a statistical approach introduced by (Chavez et al., 1982) to select the most informative six color bands composites. The index is given by the following formula:

$$OIF = \Sigma s_i / \Sigma I r_j I$$

Where (s_i) is the standard deviation for band, r_j is the correlation coefficient between any two of the three bands being evaluated.

The covariance matrix and correlated coefficient matrix of every two bands were calculated. The results are shown in Tables (1 & 2). The OIF value of the seven reflected bands of Landsat-8 is calculated and the results are listed in Table (3).

Bands 7, 5, 1 in RGB (Fig. 13) is the most informative color composite with OIF rank = 71.10 highlighting differences between the different rock units and facilitating geologic mapping of them. The image could discriminate the serpentinites, younger granites, metavolcanics and metasediments in blue, yellow, deep brown and pale purple colors respectively.

Band ratios exaggerate lithological discrimination due to each mineral has its own characteristic spectral absorption features. Serpentinite and argillic zone indicated by us-

Table 1: Band covariance matrix of study area

	b1	b2	b3	b4	b5	b6	b7
b1	3437.68						
b2	3419.54	3410.8					
b3	3409.29	3407	3474.01				
b4	3240.32	3243.1	3403.43	3566.83			
b5	3023.66	3031.52	3246.21	3557.36	3688.52		
b6	2890.91	2903.07	3110.11	3394.49	3523.23	3721.28	
b7	2680.77	2693.51	2853.6	3047.49	3127.42	3432.92	3448.56

Table 2 : Band correlation matrix of study area

	b1	b2	b3	b4	b5	b6	b7
b1	1.00						
b2	1.00	1.00					
b3	0.99	0.99	1.00				
b4	0.93	0.93	0.97	1.00			
b5	0.85	0.85	0.91	0.98	1.00		
b6	0.81	0.81	0.86	0.93	0.95	1.00	
b7	0.78	0.79	0.82	0.87	0.88	0.96	1.00

Table 3: The OIF of study area image

	R	G	B	Rank
1	b7	b5	b1	71.10
2	b7	b5	b2	70.67
3	b7	b6	b1	70.08
4	b7	b6	b2	69.62
5	b6	b5	b1	69.15
6	b7	b4	b1	68.83

ing the band ratios 6/7 (Fig. 14). The choice of this ratio is based on that the OH-bearing minerals have a strong reflection in band 6, and show a great absorption feature in band 7 between 2.12 to 2.23µm, this absorption is due to Al-OH. Silicate minerals have absorption features in band 2 and relative reflection in band 6 (Sabin, 1999; Safari et al., 2017). So that band ratio 6/2 used to delineate silicate minerals and phylliczone (Fig. 15). According to band ratio 6/2 image, the granitic pluton differentiated according to the silica content into two varieties. The content of silica increases towards the outer parts of the pluton (syenogranites). The discrimination of different rock units with accurate trace of their contacts has been achieved by used two band ratio images in RGB (Figs.16 & 17). The visual interpretation of them confirmed their efficiency in geologic mapping especially in high lighting the granitic rocks and serpentinites. The first false color composite image (6/2, 4/3, 6/7 in RGB), differentiated the granitic pluton in the area into two verities. The syenogranites appear as yellowish red and the monzogranites appear as brownish red. The serpentinite appears as dark blue color. The false color composite image (4/2, 5/6, 6/7 in RGB) differentiated the granitic pluton in the area into two verities. The syenogranites

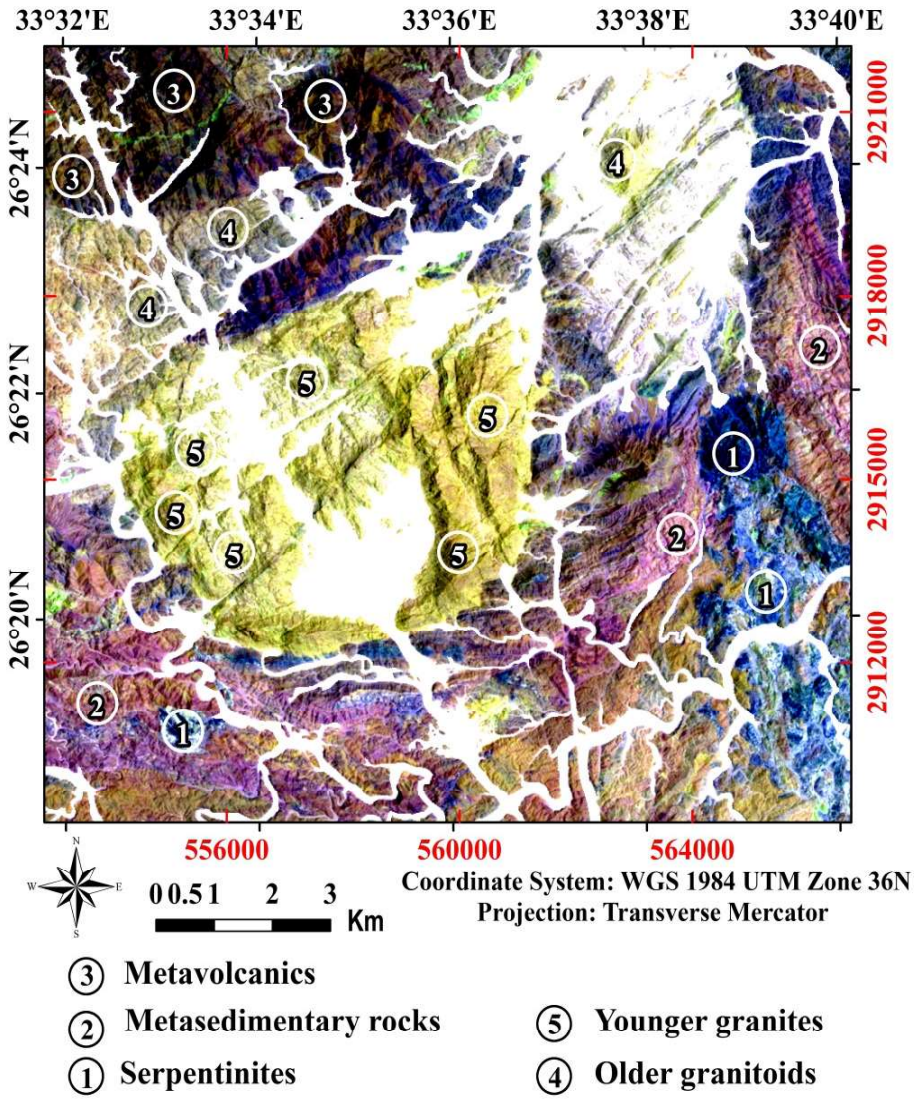

Fig. 13: False color composite image of bands 7, 5, 1 in RGB of Kab Amiri area, CED, Egypt

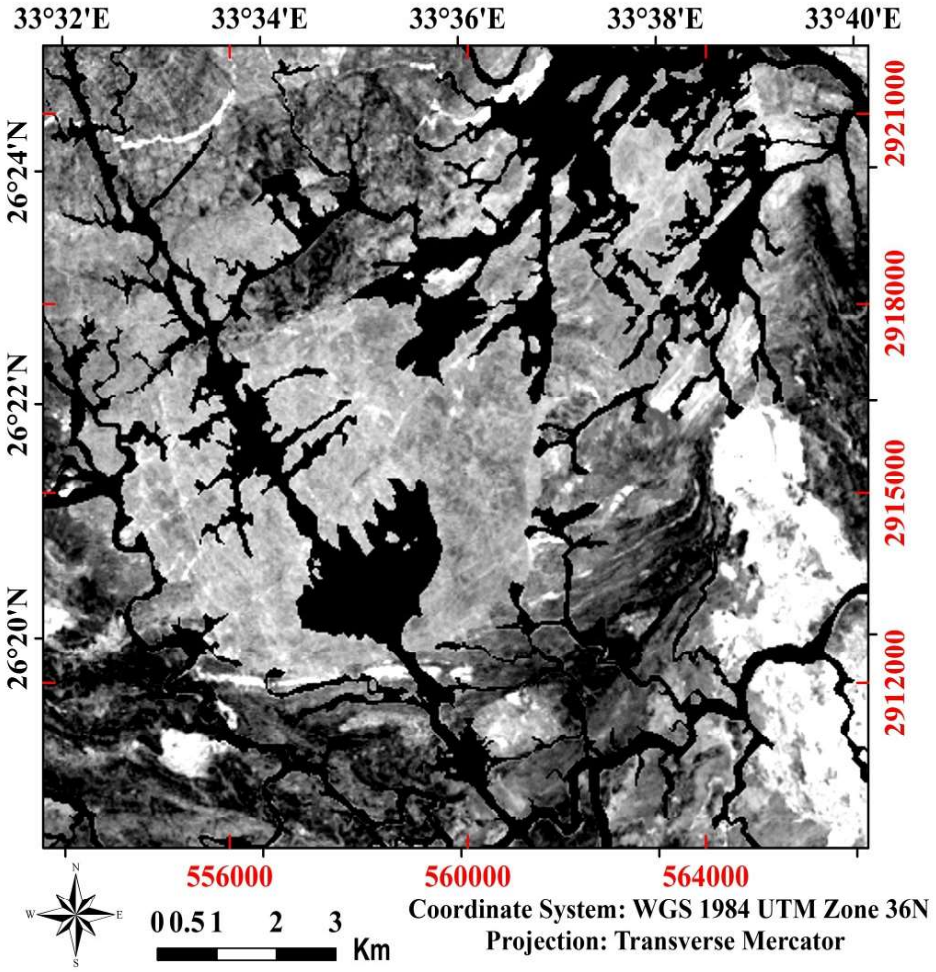

Fig. 14 : b6/b7 ratio image showing carbonates and OH-bearing minerals in brightened areas, Kab Amiri area, CED, Egypt

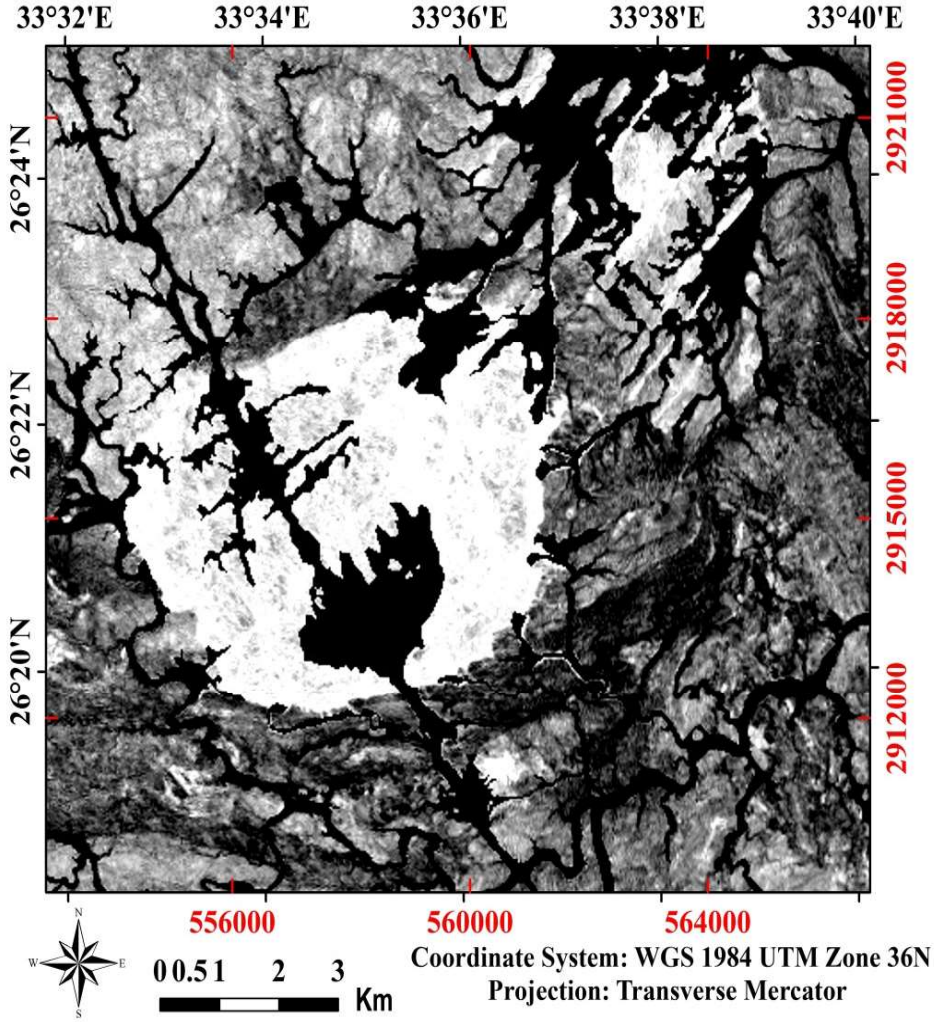

Fig. 15: b6/b2 ratio image showing silicate minerals and phyllic zone in brightened areas, Kab Amiri area, CED, Egypt

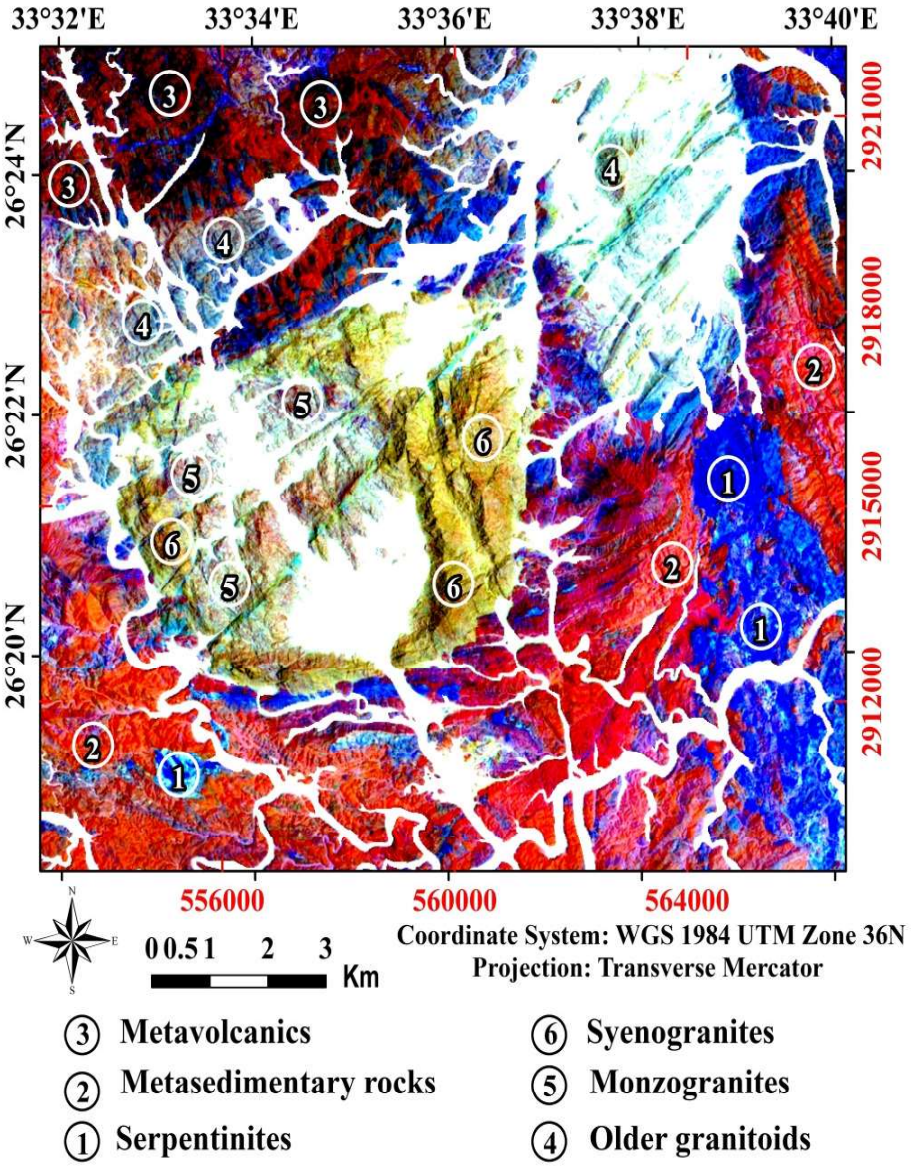

Fig. 16: Landsat-8 band ratio image (b6/b2, b4/b3, b6/b7) in RGB of Kab Amiri area, CED, Egypt

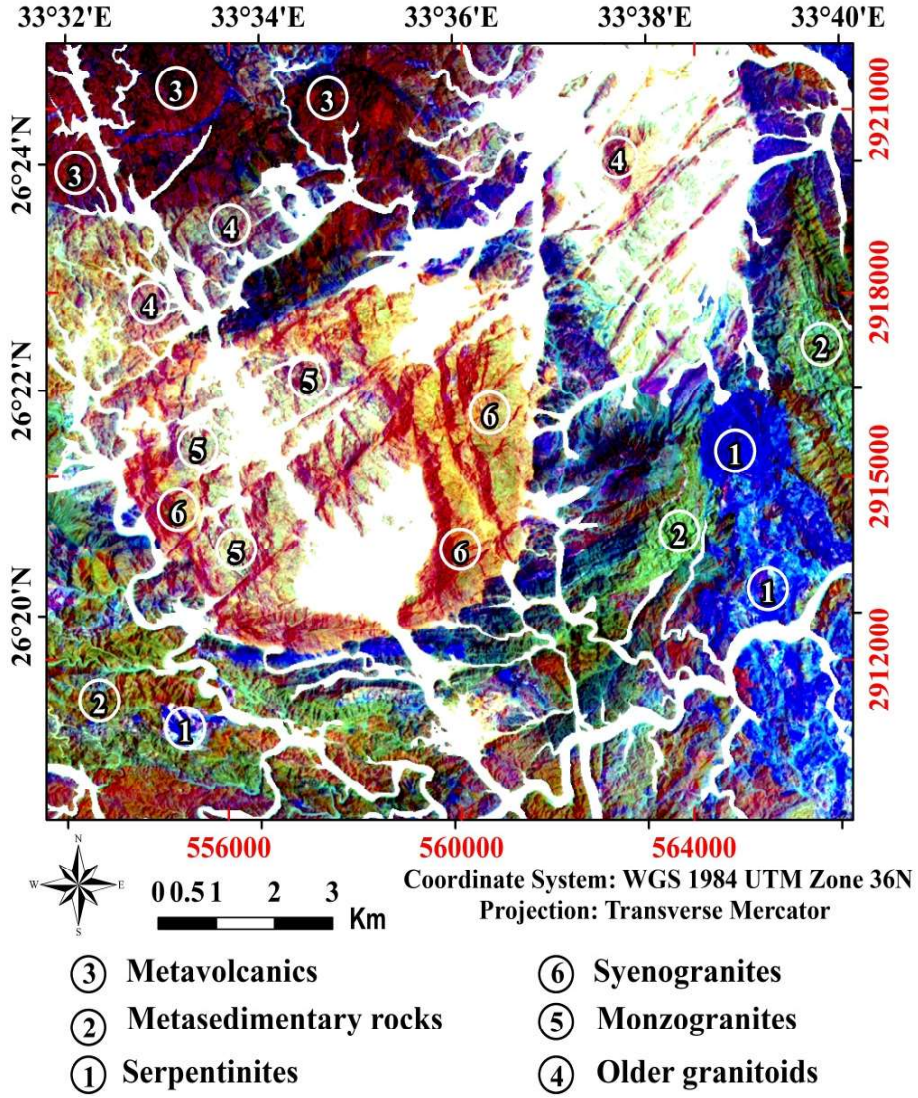

Fig. 17: Landsat-8 band ratio image (b4/b2, b5/b6, b6/b7) in RGB of Kab Amiri area, CED, Egypt

appear as yellow and the monzogranites appear as pale brownish red. The serpentinite appears as dark blue color in the two images. The metasediments appears as pale to deep green color and the metavolcanics appears as deep brown color.

The PCA transformation for the Landsat-8 seven reflected bands has been calculated with their eigen vector values as listed in Table 4. PC1 account 98.07 % of the total variance and has positive loading for all bands. PC1 mapped the albedo and topographic information (Kenea and Haenisch, 1996; Ranjbar et al., 2004). PC2 has negative signs for band 6 and band 7 indicate the contrast between the visible (VIS) and shortwave infrared (SWIR) bands. The PC3, PC1 and PC2 as Red, Green and Blue (RGB) composite image of the study area is created (Fig. 18). Principal component color composite images appear more colorful due to their uncorrelated components. As shown on Figure (18), the metavolcanics appear as dark green color, serpentinite appears in deep blue color, the older granitoids appear in pale blue color and the younger granites appear in pale green color.

The remote sensing images have been verified in the field through more than 90 ground truth area (training samples) represent all rock unites cropping out in the study area with focusing on granitic rocks. After masking Quaternary sediments (Wadis), supervised areas of interests (AOIs) are selected and controlled to the exposed basement rock units. The spectral Signatures of the selected AOIs are shown on Figure (19). The supervised classification processed using the Enhanced Maximum Likelihood (EML) method. The output is shown on Figure (20). Seven classes are given to seven colors each is corresponding to a certain rock unit. serpentinites (black), metasediments (cyan), metavolcanics (deep violet), older granitoids (yellow), monzogranites (pink), syenogranites (red) and stream sediments (white).

AIRBORNE GAMMA-RAY SPECTROMETRY

Airborne gamma-ray spectrometry measures the abundance of potassium, thorium and uranium in rocks and weathered materials by detecting gamma-ray emitted due to the natural radioelement decay of these elements. Three Radio-elements colored contour maps comprising (eU in ppm), (eTh in ppm) and (K%) are shown in (Figs. 21,22 & 23) respectively, all values are multiplied by 10**.**

The equivalent uranium (eU) contour map (Fig. 21) can be classified into three levels. The highest level of radioactivity (from bright magenta to strong magenta). This level expands from 32.5 ppm up to 80.9ppm and is essentially associated with younger granites. The intermediate level of radioactivity (from yellow to red). This level expands from 7.6 ppm up to 32 ppm and is mainly associated with the older granitoids. The metavolcanics, metasediments, serpentinites have the lowest radioactivity level (from dark blue to pale green) with values less than 7.6 ppm.

The equivalent thorium (eTh) contour map (Fig. 22) can be classified into three levels. The highest level of radioactivity (red to strong magenta). This level expands from 80 ppm up to 269.8 ppm and is essentially associated with G. Kab Amiri younger granites. The older granitoids possess the intermediate level of radioactivity (from deep yellow to pale red). This level expands from 30 ppm up to 63 ppm. The lowest radioactivity level (from dark blue to pale green) is associated with the metavolcanics, metasediments and serpentinites.

The distribution of relative potassium concentration overall the study area was illustrated as on Figure (23). The high level (>10%) is associated with the younger granites. The older granitoids possess the intermediate level from 7 to 10 %, while the serpentinites represent the lowest level (less than 7%).

The Radio-elements composite image ternary map (Fig. 24) combines the data K, eTh

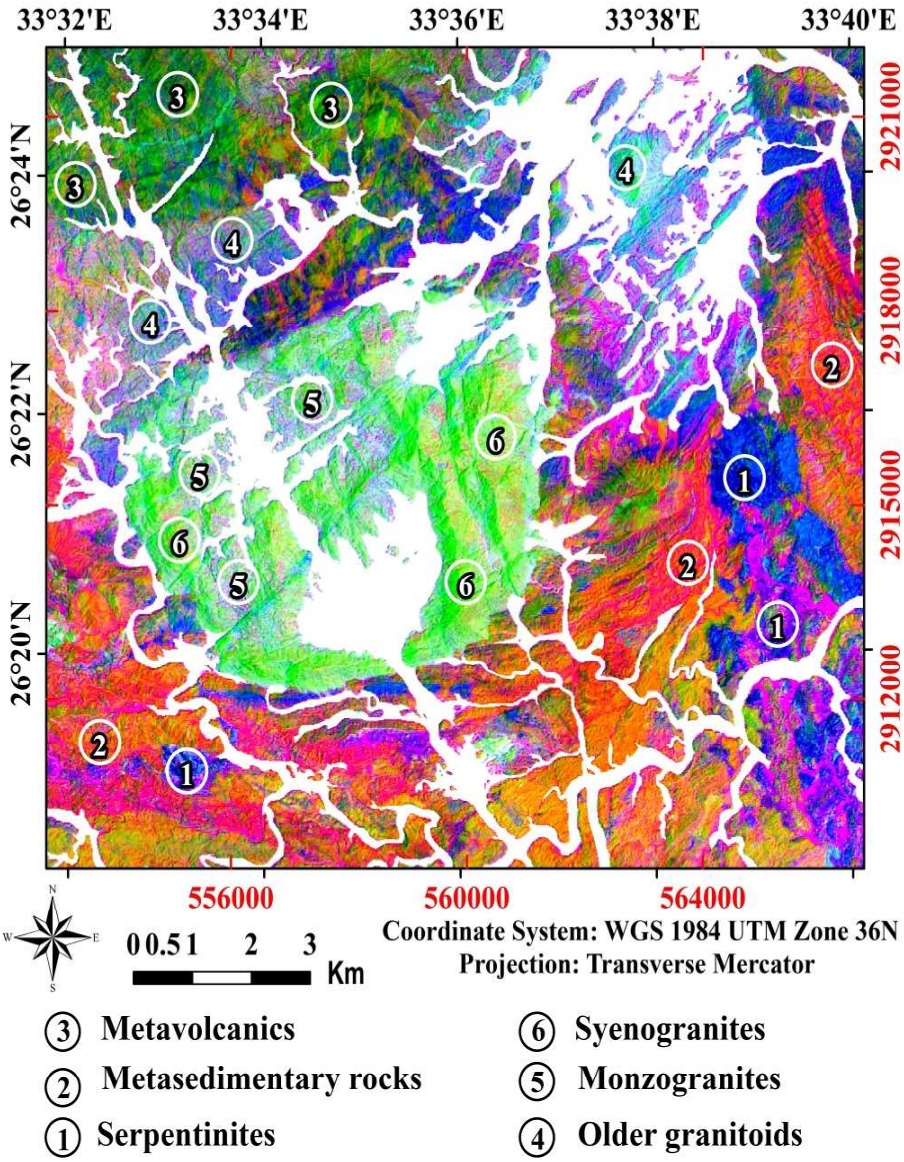

Fig. 18: Landsat-8 image of PCs (3, 1, 2) in RGB of Kab Amiri area, CED, Egypt

Table 4 : Eigenvector PCA for the first seven bands of the used landsat-8 data

Eigenvector	Band 1	Band 2	Band 3	Band 4	Band 5	Band 6	Band 7	Eigenvalue
PC 1	0.160	0.181	0.271	0.401	0.474	0.530	0.449	98.07
PC2	0.308	0.338	0.411	0.355	0.187	-0.375	-0.566	1.158
PC 3	-0.337	-0.371	-0.335	0.126	0.610	0.159	-0.472	0.639
PC 4	-0.119	-0.125	-0.091	0.157	0.360	-0.744	0.504	0.113
PC5	-0.392	-0.351	0.216	0.684	-0.457	0.019	0.000	0.017
PC 6	-0.442	-0.143	0.744	-0.448	0.171	-0.010	-0.003	0.003
PC 7	0.634	-0.746	0.190	-0.067	0.018	-0.002	0.003	0.002

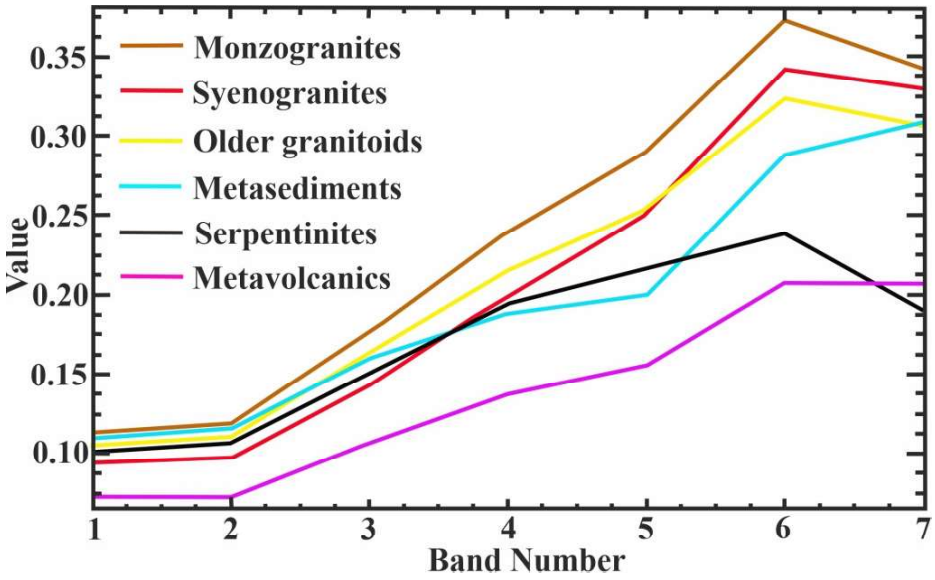

Fig. 19: The spectral profile of the end members presented to OLI band number

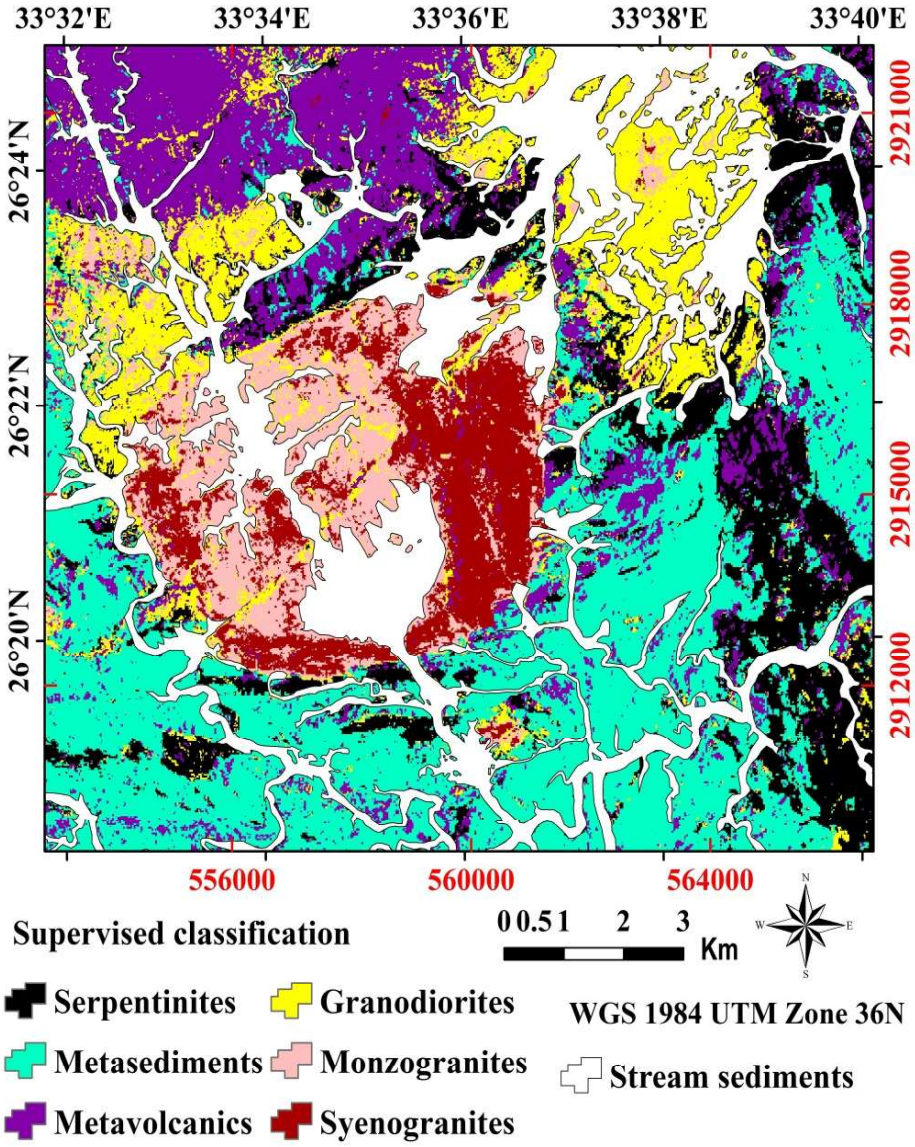

Fig. 20: Supervised classification image for Kab Amiri area, CED, Egypt

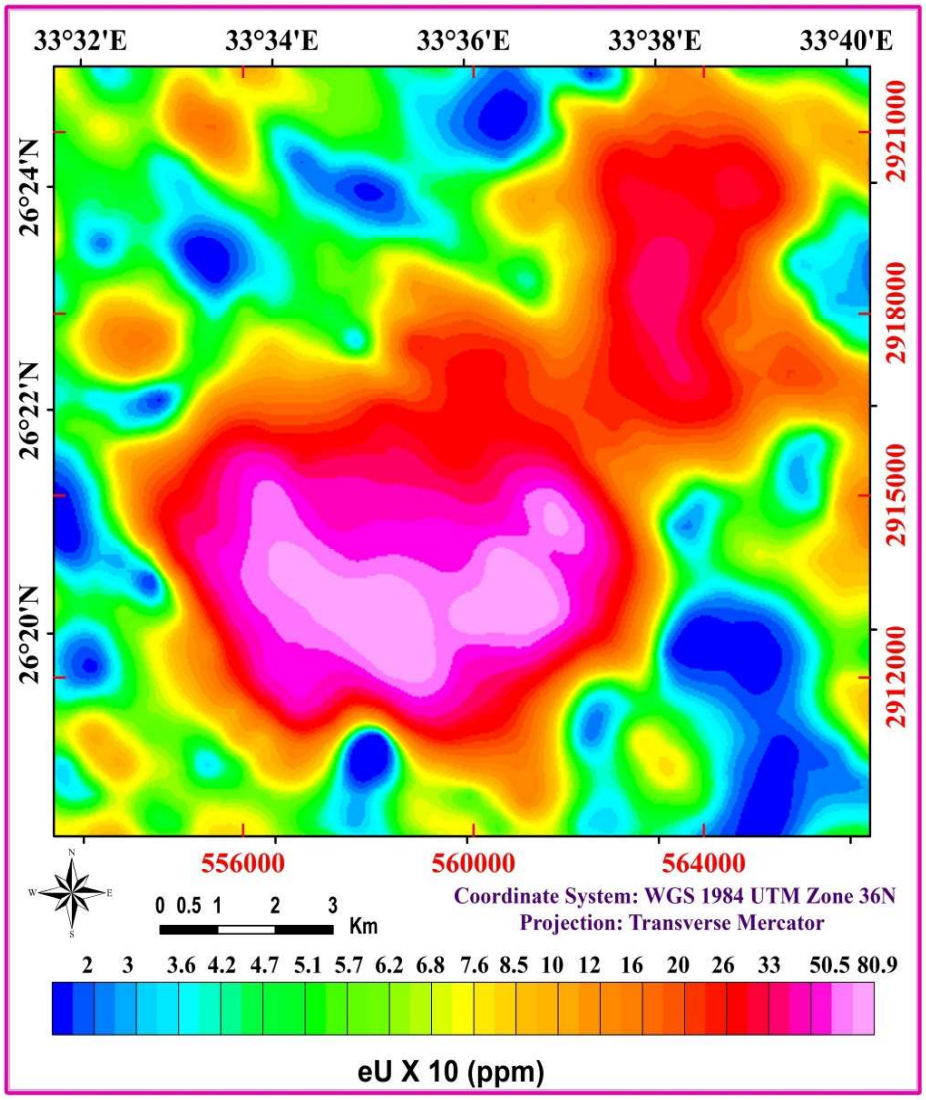

Fig. 21: Equivalent uranium contour map (ppm) of Kab Amiri area, CED, Egypt

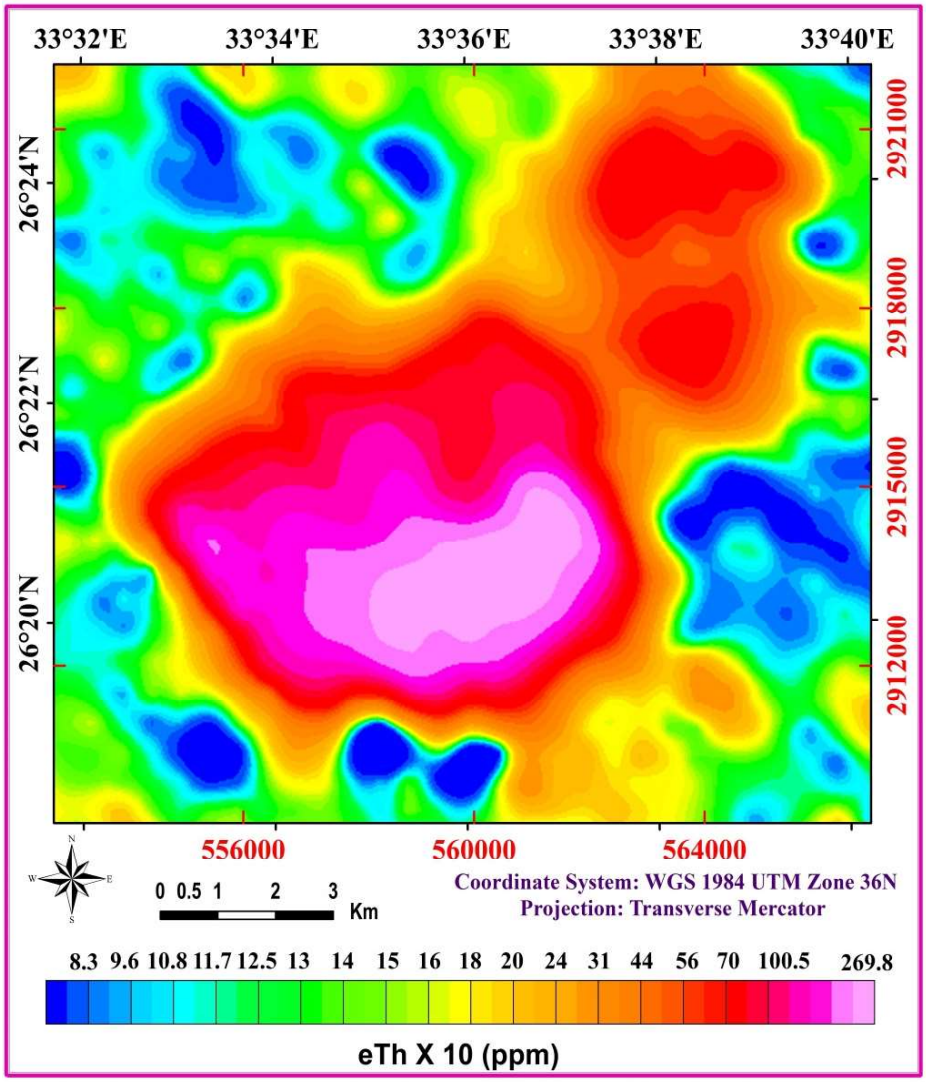

Fig. 22: Equivalent thorium contour map (ppm) of Kab Amiri area, CED, Egypt

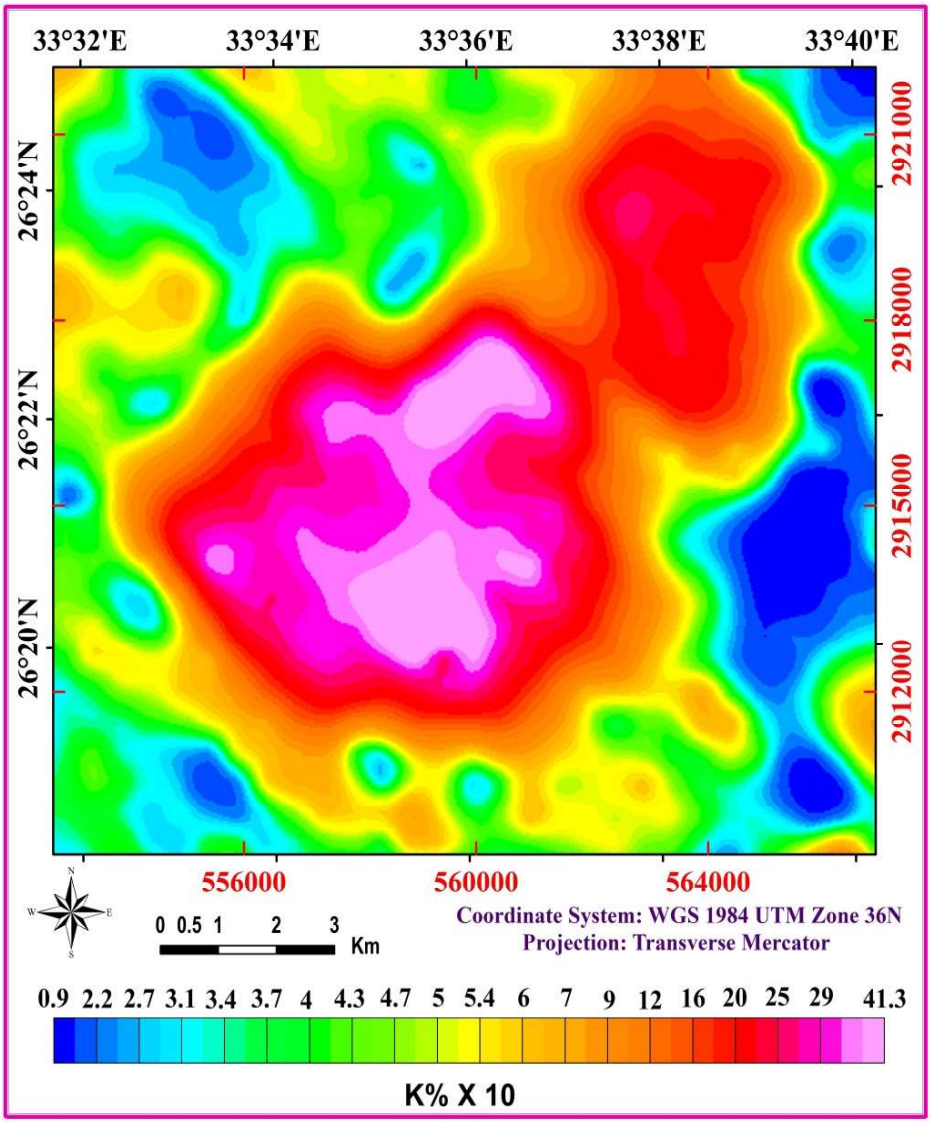

Fig. 23: Potassium contour map (%) of Kab Amiri area, CED, Egypt

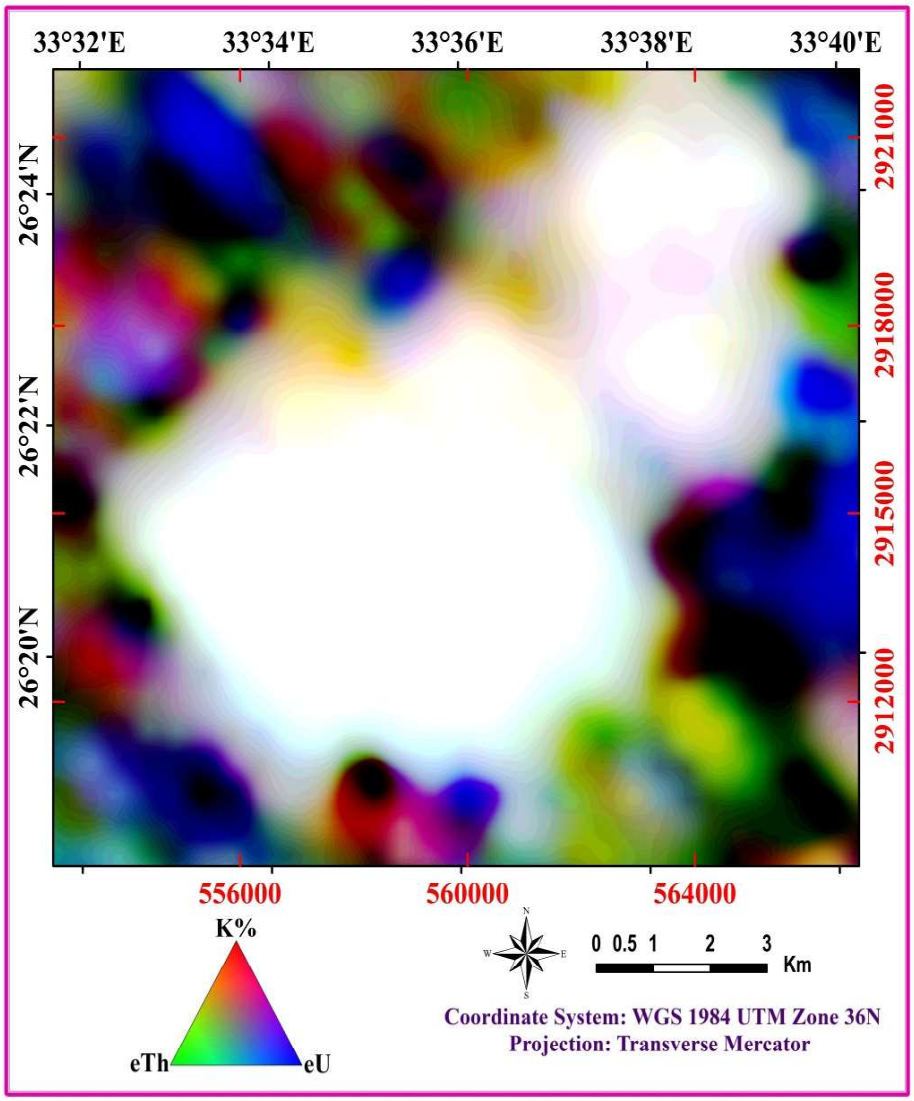

Fig. 24: Radio-elements composite image terrnary map of Kab Amiri area, CED, Egypt

and eU in RGB. From the map, it is observed that the high concentration of K, eTh and eU (white color) is great correlated with the exposure of G. Kab Amiri younger granites at the center of the study area. In addition, the older granitoids at G. Abu Qarahish at the northeastern part of the area.

The airborne gamma-ray spectrometric data for both younger granites and granodiorites were subjected to primary statistical treatment in order to determine their distribution characteristics in the study area, whereas those of the serpentinites, metasediments and metavolcanics were excluded because of their low radioactivity level. Descriptive statistical analysis of the younger granites and older granitoids is shown in Table (5). The average radioactive contents of eU and eTh are about 40.2 ppm, 126 ppm respectively in the younger granites (Fig. 25). Noteworthy, the inner zone of granitic pluton (monzogranites) has many intrusions and offshoots of syenogranites so that quantitative interpretation was carried out for the younger granites as one rock unit. The contents of eU and eTh are about 22.87 ppm, 56.5 ppm respectively in the older granitoids (granodiorites), (Fig. 26). Because of its small area,the younger granite body that is cropping out at the southeastern side of Kab Amiri pluton does not subjected to quantitative interpretation.

Normally, thorium is three times as abundant as uranium in rocks (Rogers and Adams, 1969). When this ratio is disturbed, it indicates a depletion or enrichment of uranium. The Kab Amiri younger granites show eTh/eU average ratios slightly higher than three (3.34) suggesting slight uranium depletion. On the other hand, granodiorites show eTh/eU average ratios lower than three (2.7) suggesting slight uranium addition.

Table 5: eU, eTh, K and eTh/eU of the younger granites and older granitoids of Kab Amiri area, CED, Egypt

Rock type / Contents		Younger granites (N=125)	Older granitoids (N=64)
eU(ppm)	Minimum	3	3.8
	Maximum	79.5	27.3
	Average	40.2	15.5
eTh(ppm)	Minimum	19	31
	Maximum	265	77
	Average	126	56.5
K(%)	Minimum	5	8.5
	Maximum	41	25.9
	Average	27.3	18.1
eTh/eU	Minimum	1.6	1.33
	Maximum	5.83	4.43
	Average	3.34	2.71

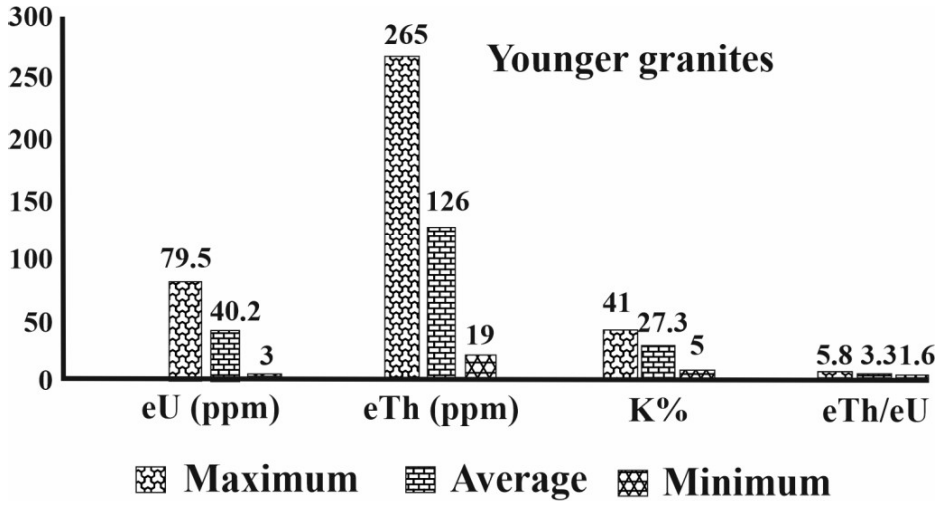

Fig. 25: Bar diagram showing minimum, maximum and averages of eU, eTh, K and eTh/eU in the younger granites of Kab Amiri area, CED, Egypt

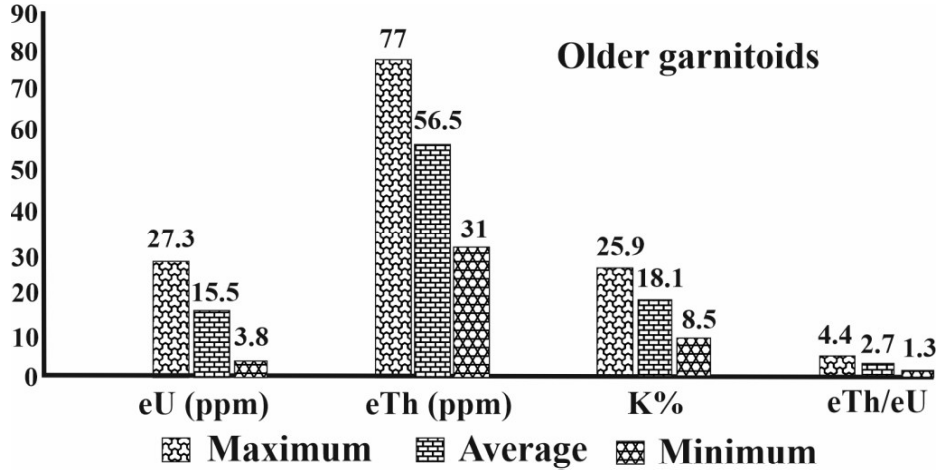

Fig. 26: Bar diagram showing minimum, maximum and averages of eU, eTh, K and eTh/eU in the older granitoids of Kab Amiri area, CED, Egypt

PETROGRAPHIC AND MINERALOGICAL INVESTIGATIONS

Petrographic investigation of seventeen thin sections, representing the younger granitic pluton as well as the older granitoids, were selected for determining the volume percentage of the rock forming minerals in the studied rock types. Table (6) shows the mineral constituents of these granitic samples. According to the modal classification of (Streckeisen, 1976), the older granitoids plot in the granodiorite field, whereas the younger granites plot in the fields of monzogranite and syenogranite (Fig. 27).

The older granitoids are mainly represented by granodiorites of hypidiomorphic texture and are mainly composed of plagioclase, quartz, K-feldspars, biotite and hornblende. Sphene, zircon and iron oxides are the main accessory minerals. Plagioclase represents the main mineral constituent in granodiorite. It occurs as euhedral to subhedral prismatic crystals. Their crystals exhibit albite, carlsbad and combined albite-carlsbad twinning as well as zoning. Plagioclase crystals are partially saussuritized and altered to clay minerals. Quartz occurs as anhedral crystals varying in size from small interstitial grains to large engaged crystals (up to 3.5 mm). Alkali-feldspars are represented by orthoclase and orthoclase perthite. Biotite is pleochroic from yellowish green to dark brown. Biotite shows different degrees of chloritization and segregation of iron oxides along cleavage planes. Sometimes biotite is completely altered to chlorite. Hornblende occurs as prisms and sometimes in the rhomb shape with green color and mostly tend to be replaced by biotite and/or chlorite. Sphene occurs as sphenoidal form. It is fairly pleochroic from pale brown to reddish brown.

The monzogranites are mainly equigranularbut sometimes porphyritic. They are mainly composed of quartz, plagioclase, K-feldspars and biotite. Chlorite and muscovite are secondary minerals. Zircon, apatite and opaques are the main accessory minerals. Quartz is the most dominant mineral. It occurs as anhedral to subhedral crystals ranging in size from 0.7mm to 3.8mm across. It corrodes the plagioclase and potash feldspars (Fig. 28). Sometimes, they exhibit undulose extinction due to strain effects especially near fault planes. Plagioclase occurs as euhedral to subhedral prismatic crystals, showing Carlsbad and lamellar twinning (Fig. 29). Potash feldspars occur as subhedral to anhedralcrystals of microcline and orthoclase perthites. Microcline is characterized by the cross-hatching twinning(Fig. 30). Biotite flakes usually appear corroded by quartz and plagioclase;they show different degrees of chloritization (Fig. 31). Both euhedral zircon and apatite are encountered as accessory minerals(Figs. 32 & 33).

The syenogranites are mainly composed of K-feldspars, quartz and plagioclase with biotite and muscovite as essential minerals. Garnet, fluorite, allanite and zircon are accessory minerals. K-feldspars are the most dominant minerals mainly represented by microcline perthite and perthite. Quartz ranks second in abundance and is found in two forms. The first is a very small interstitial crystal between feldspar crystals (Fig. 34), while the second occurs as anhedral to subhedral crystals ranging in size from 0.5 mm to 2.9 mm across. Plagioclase occurs as euhedral to subhedral prismatic crystals of about 0.7mm in width and 1.8mm in length, showing lamellar, Carlsbad twinning. Plagioclase is corroded by K-feldspars and quartz. Biotite occurs as anhedral to subhedral flakes partially altered to chlorite. Muscovite occurs as primary irregular large flakes(Figs. 35 and 36). Garnet, colorless fluorite, allanite and zircon are recorded as accessory minerals (Figs. 37, 38 & 39).

The mineralogical study of the black metallic minerals collected from the pegmatitesat the contact between the syenogranites and monzogranites was performed using the Environmental Scanning Electron Micro-

Table 6: Modal analysis of the granitic rocks of Kab Amiri area, CED, Egypt

	Sample No.	Mineral constituents					Total
		Quartz	Alkali-feldspars	Plagioclase	Micas	Accessories	
Younger granites	1	30.3	38.0	26.1	4.3	1.3	100
	2	39.4	26.4	27.5	4.8	1.9	100
	3	36.2	30.4	28.3	4.1	1.0	100
	4	43.8	28.1	23.2	3.4	1.5	100
	5	35.6	31.1	26.2	5.7	1.4	100
	6	29.3	32.0	34.2	3.2	1.3	100
	7	32.5	47.0	16.7	3.0	0.8	100
	8	31.0	45.1	18.1	4.3	1.5	100
	9	32.5	36.7	25.7	4.0	1.2	100
	10	30.1	43.5	21.2	4.0	1.2	100
	11	37.4	29.3	28.0	4.2	1.0	99.9
	12	33.0	41.1	20.2	4.3	1.3	99.92
	13	29.3	42.5	19.2	6.3	2.7	100
Older granitoids	14	23.4	12.0	48.2	13.5	2.9	100
	15	26.2	9.3	52.1	9.0	3.4	100
	16	24.5	14.5	46.5	11.3	3.2	100
	17	23.5	13.5	50.4	8.5	4.1	100

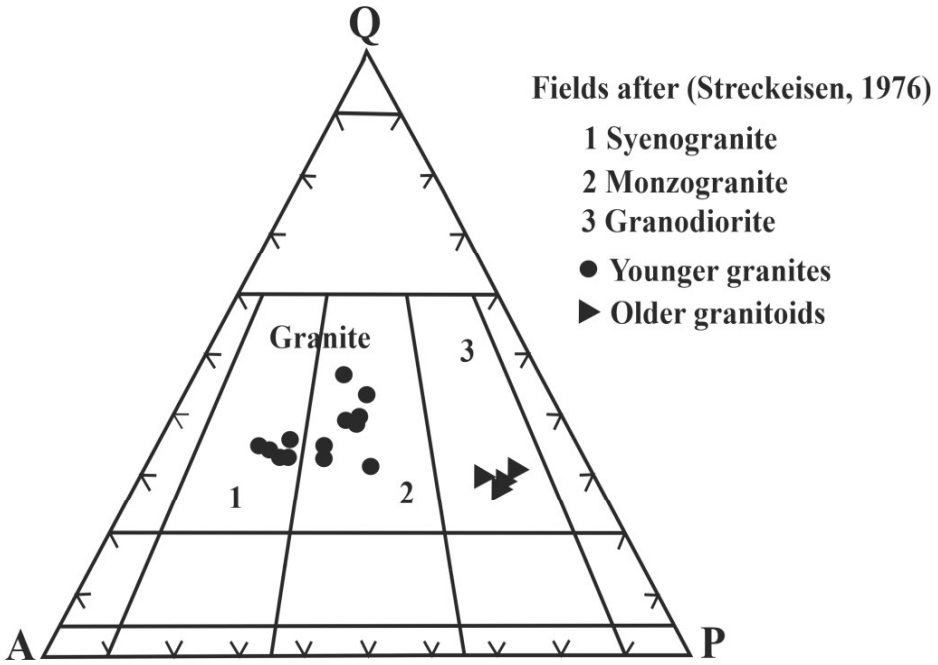

Fig. 27: Modal composition for the granitic rocks of Kab Amiri area, CED, Egypt (After Streckeisen, 1976)

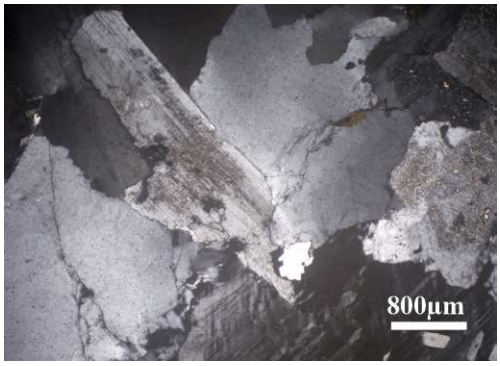

Fig. 28: General view showing partially altered plagioclase, K-feldspar, and quartz, Gabal Kab Amiri monzogranites, XPL

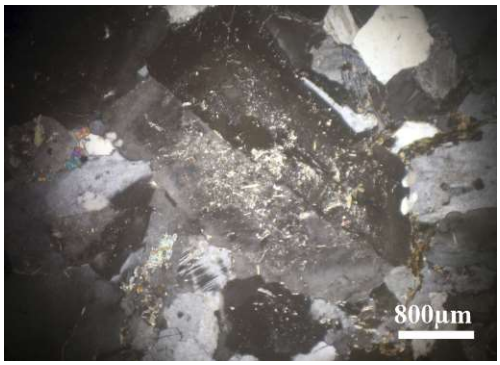

Fig. 29: Saussuritized zoned plagioclase crystal showing simple twinning, Gabal Kab Amiri monzogranites, XPL

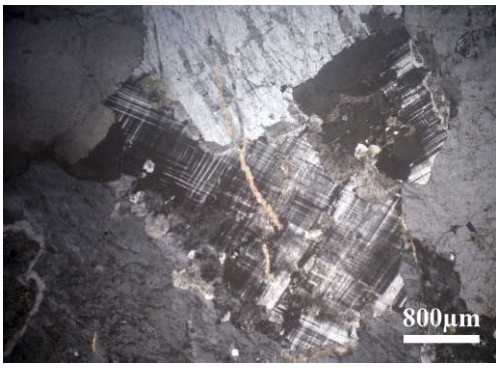

Fig. 30: Microcline and orthoclase perthite, Gabal Kab Amiri monzogranites, XPL

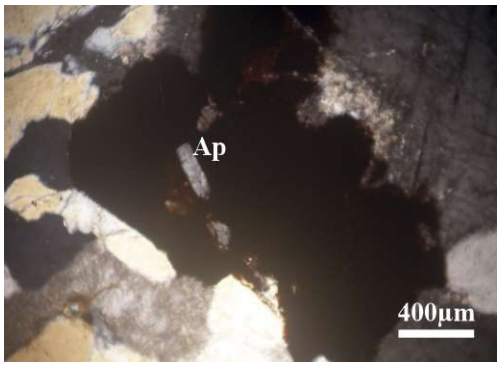

Fig. 33: Euhedral crystal of apatite(Ap) included in obaques (iron oxide), Gabal Kab Amiri monzogranites, XPL

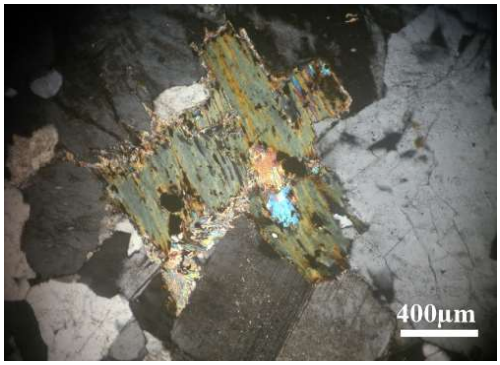

Fig. 31: Highly chloritzed biotite with relicts of muscovite, Gabal Kab Amiri monzogranites, XPL

Fig. 34: String and patchy-type perthites slightly sericitized, Gabal Kab Amiri syenogranites, XPL

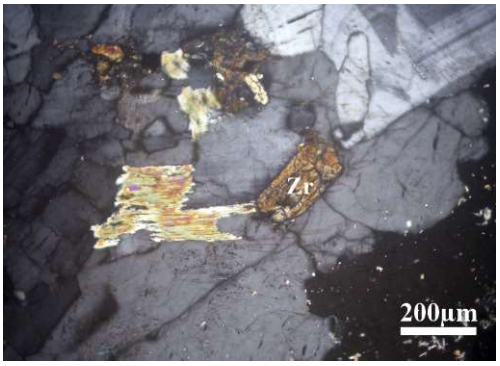

Fig. 32: Metamected zircon (Zr) associated with Quartz , plagioclase and biotite, Gabal Kab Amiri monzogranites, XPL

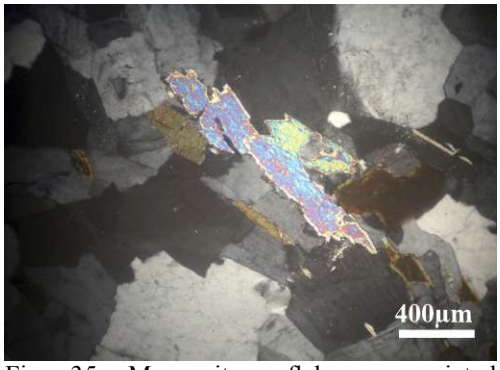

Fig. 35: Muscovite flake associated with quartz and Biotite, Gabal Kab Amiri syenogranites, XPL

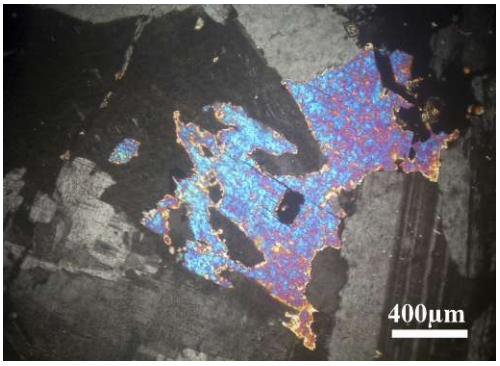

Fig. 36: Muscovite corroding perthite,Gabal Kab Amiri syenogranites, XPL

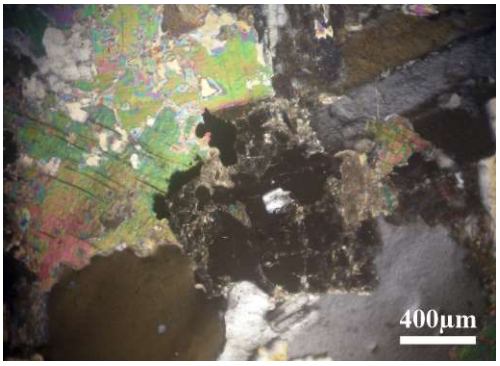

Fig. 37: Garnet associated with biotite and plagioclase, Gabal Kab Amiri syenogranites, XPL

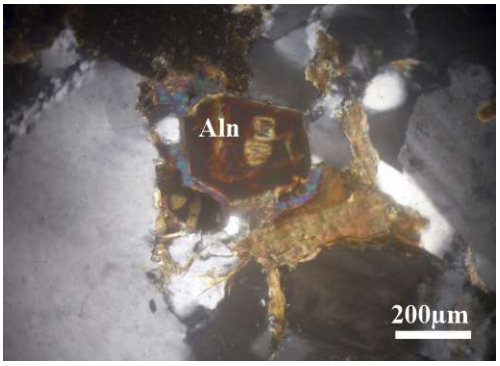

Fig. 38: Euhedral crystal of allanite (Aln) in biotite and muscovite, Gabal Kab Amiri syenogranites, XPL

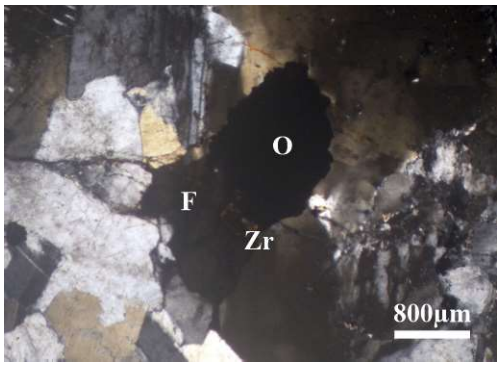

Fig. 39: Colourless flourite (F) associated with opaques(O) and metamecited zircon (Zr), Gabal Kab Amiri syenogranites, XPL

scope (ESEM) at the laboratory of Nuclear Materials Authority (NMA). The identified minerals are briefly described at the following paragraphs:

Fergusonite (Y, REE) (Nb, Ta, Ti) O_4

Fergusonite presents in the form of tabular prismatic shape (Fig. 40), which containing potential concentration of the high field strength elements (HFSE) such as Nb, Ta, and Ti, besides U.

Uranothorite (Th, U) SiO_4

Uranothoriteis a variety of thorite. It is a radioactive mineral that consists mainly of Thand U silicatespresent in amounts up to 10% (Heinrich, 1958). Uranothorite found as fine opaque inclusions on the surface of fergusonite (Fig. 41).

CONCLUSIONS

The application of image processing techniques of Landsat-8 proved its capability in lithological discrimination. Optimum Index Factor (OIF) and data transformation techniques such as band ratios (BR) and principal component analysis (PCA) high lighting the subtle spectral differences between different rock units within the study area and facilitate

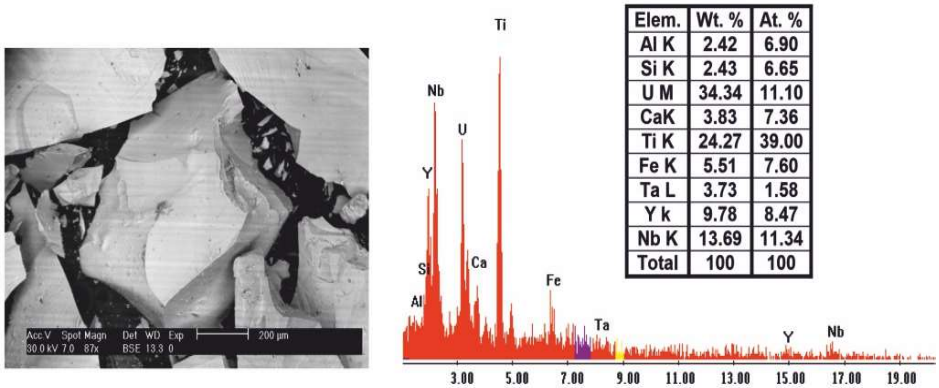

Elem.	Wt. %	At. %
Al K	2.42	6.90
Si K	2.43	6.65
U M	34.34	11.10
CaK	3.83	7.36
Ti K	24.27	39.00
Fe K	5.51	7.60
Ta L	3.73	1.58
Y k	9.78	8.47
Nb K	13.69	11.34
Total	100	100

Fig. 40: BSE image and its Semi-quantitative EDX analysis of fergusonite mineral in anomalous pegmatite

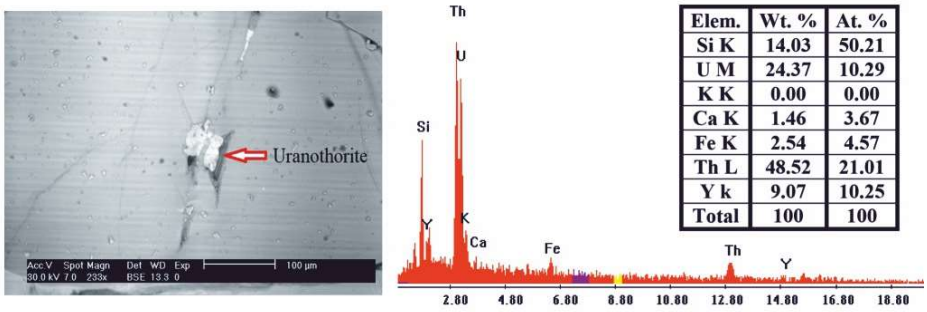

Elem.	Wt. %	At. %
Si K	14.03	50.21
U M	24.37	10.29
K K	0.00	0.00
Ca K	1.46	3.67
Fe K	2.54	4.57
Th L	48.52	21.01
Y k	9.07	10.25
Total	100	100

Fig. 41: BSE image and its Semi-quantitative EDX analysis of uranothorite mineral in anomalous pegmatite

the visual interpretation. The false color composite image of bands (7, 5, 1 in RGB) with high OIF rank value enhanced visualization of the lithological units in the study area. The band ratios [(4/2, 5/6, 6/7), (6/2, 4/3, 6/7)] are successful in differentiating the younger granites of G. Kab Amiri into two varieties (monzogranites and syenogranites) and well discriminate the other rock units. The uncorrelated components (PC3, PC1 and PC2 in RGB) success in discriminate serpentinites, metasediments, metavolcanics, granodiorites but failed in differentiate younger granites into their varieties.

The airborne radiometric data contribute in the lithological mapping of the exposed rock units. The radio-elements contour images as well as radio-elements composite image ternary map could well discriminate the younger granites and older granitoids (relatively higher radioactivity) from the other rock units (relatively lower radioactivity). Nevertheless, the images could not well discriminate between the two varieties of the younger granites because the monzogranites have many intrusions and offshoots of syenogranites. The anomalous zones are restricted to the pegmatites that occurred along the monzogranite-syenogran-

ite contacts, which comprising fergusonite and uranothorite as rare earth elements and radioactive minerals.

Based on the fieldwork verification, petrographic investigations, landsat-8 image processing, spatial distribution and contact relationships, the main rock units of the study area are represented by ophiolitic mélange (rock fragments of serpentinites in a matrix of metasediments), metavolcanics, older granitoids (granodiorites), younger granites (monzogranites and syenogranites) and basic dykes and pegmatites. The mineralogical study of the black metallic minerals collected from the pegmatites revealed the presences of fergusonite and uranothorite.

The integration of Landsat-8 images and airborne radiometric data followed by field observations and petrographic study resulted in a geologic map of scale1:50,000 (Fig. 42) with an accuracy 85.24% with a kappa coefficient value of 0.825.

REFERENCES

Abdeen, M.M.; Thurmond, A.K.; Abdelsalam, M., and Stern, B., 2001. Application of ASTER band-ratio images for Geologic mapping in arid regions; The Neoproterozoic Allaqi Suture. Egypt. Geol. Soc. Am., 33, 1-289.

Abdel Ghani, I.M., 2020. The application of Landsat-8 imagery and airborne Gamma-ray spectrometric data for lithological mapping of GabalNuqara area, Central Eastern Desert, Egypt. J. North for Basic and Applied Sciences (JNBAS),5 (1), 47-69.

Abdel Meguid, A.A., 1992. Late Proterozoic Pan African tectonic evolution of the Egyptian part of the Arabian Nubian Shield. M. E. R. C. Ain Shams Univ., Earth Sc. Ser., 6, 13-28.

Abdel Meguid, A.A.; Ammar, S.E.; Ibrahim, T.M.M.; Ali, K.G.; Shahin, H.A.; Omer, S.A.; Gaafar, I.M.E.; Masoud, S.M.; Khamis, A.A.; Haridy, M.H.; Kamel, A.I.; Mostafa, B.M.; Abo Donia, A.; Abdel Gawad, A. E., and Aly, E.M., 2003. Uranium potential of Eastern Desert granites,Egypt. NMA internal report for project: EGY/03/014 technical Assistance byIAEA 270 p.

Abdelsalam, M.G.; Stern, R.J.andBerhane, W.G., 2000. Mapping gossans in arid regions with Landsat TM and SIR-C images: the Beddaho Alteration Zone in northern Eritrea. J. Afr. Earth Sci., 30, 903-916.

Aero-Service, 1984. Final operational report of airborne magnetic/ radiation survey in the Eastern Desert, Egypt, for the Egyptian General Petroleum Cooperation. Aero Service, Houston, Texas, six volumes.

Ammar, S.E., 1993. Geological, structural, and geochemical investigations of Kab Amiri-Wadi El Saqia area and its radioactive occurrences, Central Eastern Desert, Egypt. Ph.D. Thesis, Fac. Sci., Cairo Univ., Egypt, 285p.

Azzaz, S.A.; Arnous, M.O.; Elmowafy, A.A.; Kamar, M.S., and Abdel Hafeez, W.M., 2018. Lithological discrimination and mapping using digital image processing, petrographic and radioactive investigation of Wadi Dahab area, Southeastern Sinai, Egypt. Middle East J. Applied Sciences, 8(2), 444-464.

Badr, Y.S., 2017. Application of remote sensing technique in geologic mapping of hydrothermal alteration zones and possible radioactive potentialities at RasBarud-Um Tagher area, North Eastern Desert, Egypt. Ph.D. Thesis, Fac.Sci., Menoufiya Univ., Egypt, 164p.

Bishta, A.Z., 2004. Lithologic discrimination of GabalQattar-Um Disi environs, North Eastern Desert of Egypt using thematic mapper data of Landsat 7. Proc. 3rdInter. Symposium on Geophysics, Tanta, 541-557.

Cathelineau, M., 1986. The hydrothermal alkali metasomatism effects on granitic rocks:Quartz dissolution and related subsolidus changes. J. Petrology, 27 (4), 965p.

Chavez, P.S.J.; Berlin, G.L., and Sowers, L.B., 1982. Statistical methods for selecting Landsat-MSS ratios. J. Applied Photogrammetric

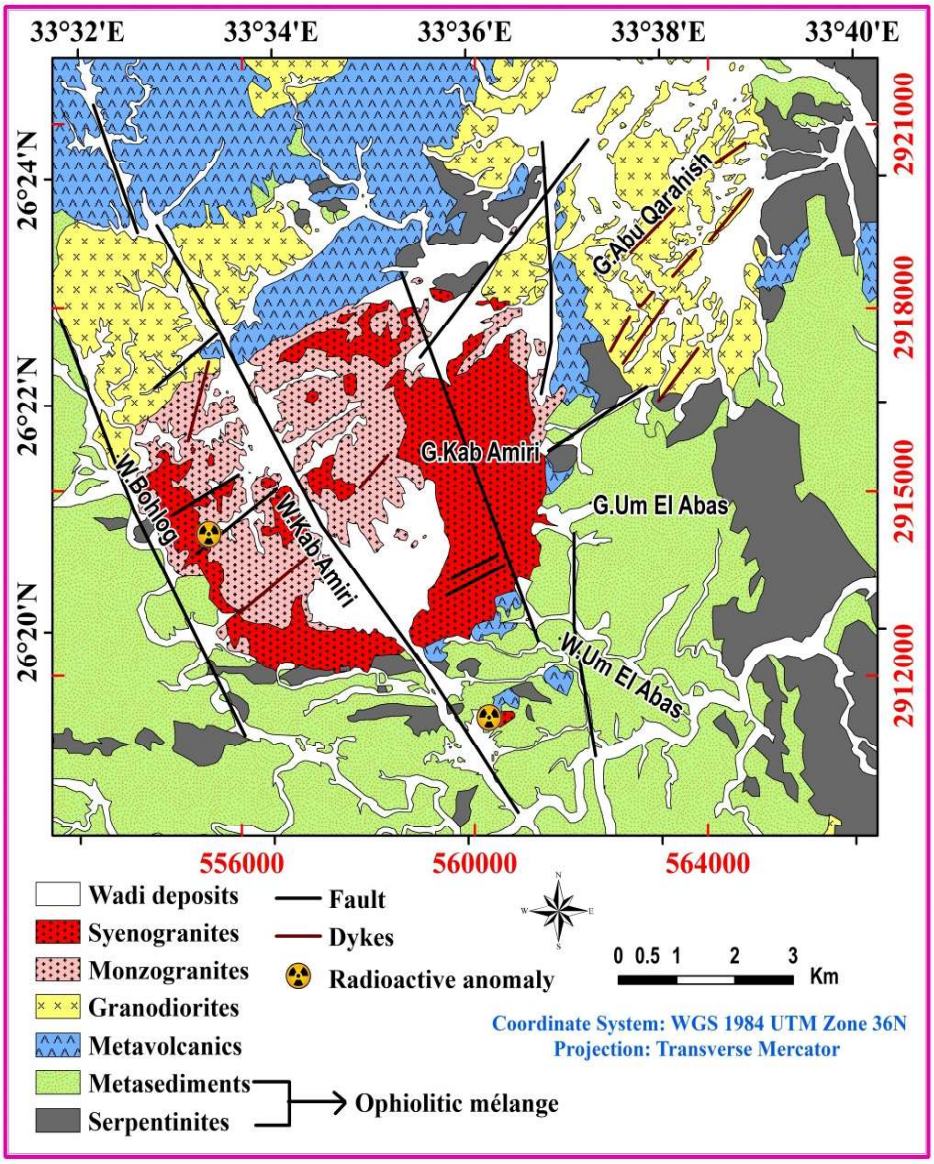

Fig. 42: Detailed geologic map for Kab Amiri area, produced from the data integration of field observations, landsat-8 image processing and petrographic studies as well as airborne gamma ray spectrometry

Engineering,8, 23-30.

Dawoud, M.; Abdel Ghani, I.M.; Elsaid, M., and Badr, Y.S., 2017. The integration of ASTER imagery and airborne gamma-ray spectrometry in lithological discrimination of Ras Barud-Um Tagher area, north Eastern Desert, Egypt. Inter. J. Innovative Science, Engineering & Technology, 4 (9), 9-23.

Di Tommaso, I., and Rubinstein, N., 2007. Hydrothermal alteration mapping using ASTER data in the Fiernillo porphyry deposit, Argentina. Ore. Geol. Rev., 32, 275-290.

El Ramly, M.F.; Greiling, R.O.; Rashwan, A.A., and Rasmy, A.H., 1993. Geologic map of Wadi Hafifit area. Scale 1: 100:000, Egy. Geol. Surv., 68p.

El-Rakaiby, M., 1993. Igneous rock-type discrimination from ratioed Landsat Thematic Mapper images of Southern Sinai, Egypt. Egy. J. Remote Sensing and Space Sciences, 1, 41-54.

Ferrier, G.; White, K.; Griffiths, G.; Bryant, R., and Stefouli, M., 2002. The mapping of hydrothermal alteration zones on the island of Lesvos, Greece, using an integrated remote sensing data set. Int. J. Remote. Sens., 23, 341-356.

Frei, M., and Jutz, S.L., 1989. Use of Thematic Mapper Data for the detection of gold bearing formations in the eastern desert of Egypt. Proc. 7th Thematic Conf. on Remote Sensing for Ore Exploration Geology,1157-1172.

Gabr, S.; Ghulam, A., and Kusky T., 2010. Detecting areas of high-potentialgold mineralization using ASTER data. Ore Geol. Rev.,38, 59-69.

Gad, S., and Kusky, T., 2006. Lithological mapping in the Eastern Desert of Egypt, the Barramiya area, using Landsat thematic mapper (TM). J. Afr. Earth Sci., 44, 196-202.

Goetz, A.F.H., and Rowan, L.C., 1981. Geol.Remote Sens. Sci., 211, 781-791.

Gomez, C.; Delacourt, C.; Allemand, P.; Ledru, P., and Wackerle, R., 2005. Using ASTER remote sensing data set for Geologic mapping, in Namibia. Physics and Chemistry of the Earth,30, 97-108.

Hammed, M.S.; Shallaly, N.A.; Abdel Ghani, I.M.; Badr, Y.S., and Sayed, S.A., 2020. Application of remotely sensing in the geologic and radioactive mapping of Wadi Fatirah Precambrian rocks, North Eastern Desert, Egypt. Nuclear. Sciences. Scientific. J., 9, 227-253.

Heinrich, E.W., 1958. Mineralogy and geology of radioactive raw materials. Mc Graw-Hill Book Company, I N C., New York, Toronto, London, 654p.

Kaufmann, H., 1988.Mineral exploration along the Aqaba-Levent structure by use of Landsat TM data: concepts, processing, and results. Int. J. Remote Sens., 9, 1639-1658.

Kenea, N. H., and Haenisch, H., 1996. Principal component analyses for lithologic and alteration mappings: examples from the Red Sea Hills, Sudan. Inter. Archives of Photogrammetry and Remote Sensing, 31 (B7), 271-275.

Kusky, T.M., and Matsah, M., 2003. Neoproterozoic dextral faulting on the Najd fault system, Saudi Arabia, preceded sinistral faulting and escape tectonics related to closure of the Mozambique Ocean. J. Geol. Soci., London, Special issue on "Proterozoic East Gondwana: Supercontinent Assembly and Break-up", edited by M. Yoshida, B.F. Windley, S. Dasgupta, and C. Powell, 327-361.

Loughlin, W.P., 1991. Principal Component Analysis for alteration mapping. Photogrammetric Engineering and Remote Sensing, 57, 1163-1169.

Mars, J.C., and Rowan, R.C., 2006. Regional mapping of phyllic and argillic altered rocks in the Zagros magmatic arc, Iran, using ASTER data and logical operator algorithms. Geosphere, 2(3), 161-186.

Pour, B.A., and Hashim, M., 2015. Hydrothermal alteration mapping from Landsat-8 data, SarCheshmeh copper mining district, southeastern Islamic Republic of Iran. J. Taibah

Univ. Sci., 9, 155-166.

Pournamdari, M.; Hashim, M., and Pour, B.A., 2014.Spectral transformation of ASTER and Landsat TM bands for lithological mapping of Soghan ophiolite complex, South Iran. Advances in Space Research,54, 694-709.

R.S.I., 2005. ENVI user's guide. Research System, Inc. Colorado, U.S.A., 1150p.

Ramadan, T.M; Ibrahim, T.M; Said, A., and Baiumi, M., 2013. Application of remote sensing in exploration for uranium mineralization in Gabal El Sela area, South Eastern Desert, Egypt. Egy. J. Remote Sens. and Space Sciences, 16, 199-210.

Ranjbar, H.; Honarmand, M., and Moezifar, Z., 2004. Application of theCrosta technique for porphyry copper alteration mapping, using ETM^+ data in the southern part of the Iranian volcanic sedimentary belt.J. Asian Earth Sciences, 24 (2),237-243.

Rogers, J.J.W., and Adams, J.S.S., 1969. Uranium. In: Handbook of geochemistry (Wedepohl, K. H. ,Ed.) , New York, Springer-Verlag, 4, 92 B1- 92 C10.

Rowan, L.C.; Hook, S.J.; Abrams, M.J., and Mars, J.C., 2003. Mapping hydrothermally altered rocks at Cuprite, Nevada, using the advanced space borne thermal emission and reflection radiometer (ASTER), a new satellite-imaging system. Econ. Geol., 98 (5), 1019-1027.

Sabins, F.F., 1999. Remote sensing for mineral exploration. Ore Geology Reviews, 14, 157-183.

Safari, M.; Pour, A.B.; Maghsoudi, A., and Hashim, M., 2017. Targeting hydrothermal alterations utilizing landsat-8 and ASTER data in Shahr-e-Babak, Iran. The Inter. Archives of the Photogrammetry, Remote Sensing and Spatial Information Sciences, XLII-4/W5, 153-157.

Sheffield, C., 1985. Selecting band combinations from multispectral data, Photogrammetric Engineering 6. Remote Sensing, 51 (6), 681-687.

Stern, R. J., 1979. Late Precambrian ensimatic volcanic rocks in Central Eastern Desert of Egypt. Ph.D. Thesis, San Diego Univ. of California, USA, 210 p.

Stern, R.J., 1994. Arc assembly and continental collision in the Neoproterozoic East African Orogen: Implications for the consolidation of Gondwanaland. Ann. Rev. Earth Planet. Sci., 22, 319-351.

Streckeisen, A., 1976. To each plutonic its proper name. Earth Sci. Rev., 12, 1-33.

Sultan, M.; Arvidson R.E., and Sturchio N.C., 1986. Mapping of serpentinites in the Eastern Desert of Egypt using Landsat Thematic Mapper data. Geology, 14, 995-999.

Velosky, J.C.; Stern, R.J., and Johnson, P.R., 2003. Geologic control of massive sulfide mineralization in the Neoproterozoic Wadi Bidah shear zone, Southwestern Saudi Arabia from orbital remote sensing and field studies. Precambrian Res., 235-247.

Vincent, R. K., and Thomson, F. J., 1972. Rock-Type Discrimination from Ratioed Infrared Scanner Images of Pisgah Crater, California, Science, 175, 986-988.

Vincent, R.K., 1997. Fundamentals of Geologic and Environmental Remote Sensing: Upper Saddle River, NJ: Prentice-Hall, Inc.

Yang Xu; Liu De-Chang; Zhang Jie-Lin., 2008. Ore-search information using Aster data in-Bashibulake uraniumdeposit area in Xinjiang. The Inter. Archives of the Photogrammetry, Remote Sensing and Spatial Information Sciences, XXXVIIPart B6b. Beijing.

Youssef, A.M.; Zaghloul, E.A.; Moussa, M.F., and Mahdi, A.M., 2009. Lithological Mapping Using Landsat Enhanced Thematic Mapper in the

تكامل بيانات لاندسات -8 وطيف أشعة جاما المحمولة جواً في التخريط الجيولوجي لمنطقة كب عميرى، وسط الصحراء الشرقية، مصر

ياسر صلاح بدر

الهدف الأساسي من الدراسة الحالية هو التخريط الجيولوجي لمنطقة كب عميرى، وسط الصحراء الشرقية، مصر، عن طريق تكامل بيانات القمر الصناعي لاندسات-٨ مع طيف أشعة جاما المحمولة جواً متبوعاً بالعمل الحقلي التفصيلي وكذا الدراسات الميكروسكوبية.

نتج عن التطبيقات المستخدمة لمعالجة صورة القمر الصناعي لاندسات-٨ (عامل المؤشر الأمثل، النسبة بين حزم الأطياف المتعددة، المكون الرئيسي للطيف،التصنيف المراقب) تعظيم الاختلافات الطيفية بين الوحدات الصخرية بمنطقة الدراسة مما سهل التخريط الجيولوجي لها كما تم تمييز وجود نوعين من الجرانيتات الحديثة.

أظهرت نتائج القياسات الجوية لأشعة جاما بمنطقة كب عميرى قدرة محدودة في التمييز الصخري والتخريط الجيولوجي بالمقارنة بصور القمر الصناعي لاندسات-٨، حيث تمكنت من تمييز الوحدات الصخرية ذات الاشعاعية العالية (الجرانيتات الحديثة والقديمة) مقارنة بباقي الوحدات، لكنها عجزت عن التمييز بين نوعي الجرانيتات الحديثة.

تم التحقق من جميع النتائج من خلال العمل الحقلي وكذا الدراسات الميكروسكوبية لصخور الجرانيت (القديمة والحديثة)، والتي اسفرت عن أن صخور الجرانيتات الحديثة تقع في نطاق (المونزوجرانيت والسيانوجرانيت) في حين وقعت صخور الجرانيتات القديمة في نطاق (الجرانوديوريت).

تم عمل خريطة جيولوجية تفصيلية بمقياس رسم (١:٥٠٠٠٠) وذلك إعتماداً على بيانات القمر الصناعي لاندسات-٨ مع طيف أشعة جاما المحمولة جواً متبوعاً بالعمل الحقلي التفصيلي وكذا الدراسات الميكروسكوبية. وأوضحت الدراسة ان تقنية الاستشعار من البعد وسيلة فعالة في عملية التخريط الجيولوجي كما توصي الدراسة بتطبيق نفس النهج والأسلوب على المناطق ذات الظروف المناخية المشابهة لمنطقة الدراسة.